Investigation of non-ideal effects in compressible boundary layers of dense vapors through direct numerical simulations

Tosto, Francesco; Wheeler, Andrew; Pini, Matteo

DOI
10.1063/5.0179570

Publication date
2024

Document Version
Final published version

Published in
Physics of Fluids

Physics of Fluids

RESEARCH ARTICLE | JANUARY 24 2024

Investigation of non-ideal effects in compressible boundary layers of dense vapors through direct numerical simulations

Francesco Tosto ; Andrew Wheeler ; Matteo Pini

Physics of Fluids 36, 016145 (2024)
https://doi.org/10.1063/5.0179570

Physics of Fluids ARTICLE pubs.aip.org/aip/pof

Investigation of non-ideal effects in compressible boundary layers of dense vapors through direct numerical simulations

Cite as: Phys. Fluids **36**, 016145 (2024); doi: 10.1063/5.0179570
Submitted: 3 October 2023 · Accepted: 20 December 2023 ·
Published Online: 24 January 2024

View Online Export Citation CrossMark

Francesco Tosto,[1] Andrew Wheeler,[2] and Matteo Pini[1,a)]

AFFILIATIONS

[1]Propulsion and Power, Delft University of Technology, Kluyverweg 1, 2629 HS Delft, the Netherlands
[2]Whittle Laboratory, University of Cambridge, J.J. Thomson Avenue 1, CB3 0DY Cambridge, United Kingdom

[a)]Author to whom correspondence should be addressed: m.pini@tudelft.nl

ABSTRACT

In this work, we present an investigation about the sources of dissipation in adiabatic boundary layers of non-ideal compressible fluid flows. Direct numerical simulations (DNS) of transitional, zero-pressure gradient boundary layer flows are performed for two fluids characterized by different complexity of the fluid molecules, namely, "air" and siloxane MM. Different sets of thermodynamic free-stream boundary conditions are selected to evaluate the influence of the fluid state on both the frictional loss and the dissipation mechanisms. The thermophysical properties of siloxane MM are calculated with a state-of-the-art equation of state. Results show that the dissipation due to both time-mean strain field, irreversible heat transfer, and turbulent dissipation differs significantly depending on both the molecular complexity of the fluid and its thermodynamic state. The dissipation coefficient calculated from the DNS results is then compared against the one obtained using a reduced-order model (ROM), which solves the two-dimensional boundary layer flow equations for an arbitrary fluid [M. Pini and C. De Servi, "Entropy generation in laminar boundary layers of non-ideal fluid flows," in 2nd International Seminar on Non-Ideal Compressible Fluid Dynamics for Propulsion and Power (Springer, 2020), pp. 104–117]. Results from both the DNS and the ROM show that low values of the overall dissipation are observed in the case of fluids made of simple molecules, e.g., air, and if the fluid is at a thermodynamic state in the proximity of that of the vapor–liquid critical point.

I. INTRODUCTION

The irreversible entropy generation due to viscous processes in boundary layers is one of the loss mechanisms mainly affecting the performance of internal flow devices such as turbomachines or heat exchangers. For instance, with regard to turbomachinery, viscous dissipation in boundary layers may account for up to one-sixth of the total loss in a turbine.[1] This contribution increases in compressors, where the flow becomes more prone to separation due to the presence of adverse pressure gradients. Important parameters influencing the viscous dissipation are the Reynolds and Mach number of the free stream, the regime of the boundary layer, i.e., laminar or turbulent, and the fluid thermo-physical properties.[2,3] In particular, precisely capturing the effect of the thermo-physical properties is crucial for accurately assessing losses in boundary layers of internal flow devices operating with organic compounds in either the supercritical or the dense vapor state. Notable applications include turbomachinery and heat exchangers for organic Rankine cycle turbogenerators,[4] supercritical carbon dioxide (sCO_2) power systems,[5] absorption chillers,[6] and heat pumps.[7,8]

The overall dissipation within a boundary layer flow can be estimated with the rate of entropy change $\dot{S}$ in the streamwise direction, which is proportional to the cube of the free-stream velocity.[1,9] $\dot{S}$ is often normalized to obtain the so-called dissipation coefficient, defined as

$$C_d = \frac{T_e \dot{S}}{\rho_e U_e^3}, \tag{1}$$

where T_e, ρ_e, and U_e denote the temperature, density, and velocity at the boundary layer edge, respectively. C_d depends on several boundary layer parameters by the relation

$$C_d = f(Re_\theta, M_e, H, Z_e, \gamma_{pv,e}, G_\infty), \tag{2}$$

where Re_θ is the Reynolds number based on the momentum thickness θ, $H = \delta^*/\theta$ is the shape factor, being δ^* the displacement thickness,

and G_∞ being the Grüneisen parameter at $v \to \infty$, which measures the molecular complexity of the fluid: the lower the value of G_∞, the higher the fluid molecular complexity.[10] The value of the compressibility factor $Z_e = p_e/(\rho_e R T_e)$ and that of the generalized isentropic exponent[11,12] $\gamma_{pv,e}$ in the free stream set the thermodynamic state of the fluid. Alternatively, reduced state variables $p_{r,e}$ and $T_{r,e}$ can be used for the same purpose. Notable features of the C_d are a weak dependence on both the boundary layer shape factor[13] and the streamwise pressure gradient in turbulent boundary layers.[1,13]

Unlike the skin friction coefficient C_f, defined as

$$C_f = \frac{\tau_w}{1/2 \rho_e U_e^2}, \tag{3}$$

where τ_w denotes the shear stress at the wall, C_d is a wall-normal integral-based parameter: its value thus provides information about the overall dissipation across the boundary layer thickness. For this reason, the dissipation coefficient is often used during the design of the internal flow devices, e.g., turbines or compressors, to properly quantify the viscous dissipation occurring in the proximity of the walls.[1,2] Analytical solutions and correlations for the skin friction coefficient and the dissipation coefficient in the zero-pressure gradient incompressible boundary layer flows of air modeled as a perfect gas are well established in the literature.[13] Corrections based on the value of the Chapman–Rubesin parameter[3] are defined as

$$CR_w = \rho_w \mu_w / (\rho_e \mu_e), \tag{4}$$

ρ and μ being the density and the viscosity evaluated at the wall (subscript w) and the boundary layer edge (subscript e), or the shape factor[14] are also available for the compressible flow case. Starting from the late 80s, following the pioneering work by Spalart,[15] numerous direct numerical simulations (DNS) of incompressible and compressible wall-bounded flows of air over flat plates have been performed to delve into the intricacies of turbulent flows. C_f values obtained from such high-fidelity simulations have been verified with those from the existing correlation, often resulting in a perfect agreement, see, e.g., works by Wu and Moin,[16] Pirozzoli and Bernardini,[17] and Wenzel *et al.*[18]

To the author's knowledge, there is currently no existing correlation for both skin friction and dissipation coefficients specifically tailored to zero-pressure-gradient boundary layer flows involving fluids other than air. Additionally, such correlations are lacking for fluid states that deviate from those typical of perfect gases, specifically when $Z_e < 1$. In such flow processes, the fluid thermo-physical properties can exhibit large variations that, in turn, affect the flow evolution, the turbulence dynamics, and, consequently, the viscous dissipation. The gas dynamics of such non-ideal flows is governed by the so-called fundamental derivative of gas dynamics,[19] defined as

$$\Gamma \equiv 1 + \frac{\rho}{c}\left(\frac{\partial c}{\partial \rho}\right)_s, \tag{5}$$

where ρ is the density, c is the speed of sound, and s is the entropy. Kluwick[20] first investigated the physics of the unperturbed zero-pressure gradient laminar boundary layer flow of dense vapors. His analysis showed that, for a fluid characterized by a high complexity of the molecular structure, the Eckert number evaluated at the boundary layer edge is defined as

$$Ec_e = \frac{U_e^2}{c_{p,e} T_e}, \tag{6}$$

where c_p is the specific heat at constant pressure and is much lower than unity, i.e., $Ec_e \ll 1$. For such fluids, no large gradients in temperature can thus be observed across the boundary layer. As a consequence, the thermodynamic and the kinematic fields are decoupled and compressible flow effects become less relevant than in wall-bounded flows of perfect gases. Similar findings were obtained by Cramer *et al.*,[21] who examined the validity of classical scaling laws for the skin friction coefficient in zero-pressure gradient laminar boundary layers for a range of fluids and thermodynamic states, and by Pini and de Servi,[22] who investigated the dissipation coefficient C_d in the zero-pressure gradient laminar boundary layer flows of various fluids. According to their results, for fluids made of large molecules, the values of both the skin friction and the dissipation coefficients approach those characterizing incompressible air flows.

Extending these findings to the turbulent regime required the setup of high-fidelity numerical simulations, whose results need then to be verified against experiments. In recent years, several authors investigated the homogeneous isotropic turbulence (HIT)[23–25] and the turbulence decay[26] of flows of dense organic vapors through DNS. These studies showed that the overall turbulence dynamics is primarily characterized by effects related to molecular complexity, while the small-scale dynamics can be deeply influenced by the local variations of the speed of sound or, equivalently, the fundamental derivative of gas dynamics.[19] However, properties such as the rate of the turbulent kinetic energy decay are barely affected by the type of fluid molecule. Vadrot *et al.*[27,28] investigated the effects of the thermodynamic state of fluorocarbon FC-70 on the development of a turbulent compressible mixing layer in subsonic and supersonic regimes. They found out that mixing layers flows occurring in the dilute gas and the dense vapor state display close values of the momentum thickness growth rate. However, at high supersonic Mach numbers, a decrease in the growth rate is observed when the fluid is operating in a thermodynamic state such that $\Gamma < 0$ dense gas. Sciacovelli *et al.* conducted direct numerical simulations of the channel[29] and the flat plate[30] flows of perfluoroperhydrophenanthrene PP11 at $M_e > 2$. They found that both C_f and the Nusselt number are weakly affected by compressibility effects, as the state of the dense vapor boundary layer is almost insensitive to friction heating, in line with the results by Kluwick[20] and Pini and de Servi.[22] More recently, Gloerfelt *et al.*[31] and Cinnella and Gloerfelt[32] conducted an extensive review of turbulent flows of non-ideal gases, with a focus on wall-bounded flows of an organic vapor. Noteworthy findings include the decoupling of dynamical and thermal effects, the almost suppression of thermal fluctuations, and the close resemblance of turbulent profiles to incompressible ones even at high-subsonic speeds. In particular, they found out that the first- and second-order velocity statistics remain similar to those observed in incompressible flows, although compressible flow characteristics such as the high levels of density fluctuations close to the wall and the emission of acoustic waves in the external flow are observed.

Nevertheless, none of these studies have delved into the loss accounting and the analysis of dissipation mechanisms occurring within a turbulent boundary layer flow of dense organic vapors. Although the friction coefficient values obtained from DNS at supersonic Mach numbers have shown to agree with those obtained from experimental correlations for incompressible flow, see, e.g., Sciacovelli

et al.,[29,30] no analysis regarding the dissipation coefficient is available in the literature. Moreover, in most cases, simulations were performed at highly supersonic or hypersonic Mach numbers,[29,30] or using thermodynamic models, which overestimate the degree of thermodynamic non-ideality in the proximity of the vapor–liquid critical point. Such conditions are not representative of flow processes observed in process and energy applications (for instance, those characterizing compression or expansion processes in gas turbines or ORC power systems).

The objective of this work is to investigate the sources of dissipation in the adiabatic, zero-pressure gradient boundary layer flow of fluids in the dense vapor state. Direct numerical simulations of transitional, zero-pressure gradient boundary layer flows are performed using an in-house solver. Two fluids characterized by different levels of molecular complexity are considered, namely, air and hexamethyldisiloxane (MM). Different sets of free-stream thermodynamic conditions are chosen to evaluate the influence of the fluid state on both the frictional loss and the dissipation mechanisms. State-of-the-art equations of state models[33] implemented in the REFPROP 10 software[34] are used to estimate the thermo-physical properties of siloxane MM. Results are compared against those obtained with a reduced-order model (ROM)[1,2] which solves the boundary layer equations in transformed coordinates for arbitrary fluids. The ROM is then used to perform a comprehensive study on the influence of the fluid, the thermodynamic state, and the compressibility on the dissipation of several compounds of engineering interest.

This paper is structured as follows. In Sec. II, the approach to evaluating the dissipation in a fully resolved turbulent boundary layer is discussed. The Falkner–Skan transformed boundary layer equations used to develop the reduced-order model are also documented, as well as the analytical relation for the estimation of the dissipation coefficient. Section III describes the methodology used to set up and run both the DNS and the ROM calculations. In this section, the test cases investigated in this study are also listed and discussed. In Sec. IV, the results of the study are treated. Finally, Sec. V lists the main conclusions of the work.

II. THEORETICAL BACKGROUND

A. Dissipation in turbulent boundary layer flows

One way of gaining physical insights into the dissipation occurring within a turbulent boundary layer flow is to (i) numerically resolve the small scales of the turbulent structures by performing direct numerical simulations (DNS), (ii) average the pertinent flow variables over a time span long enough to ensure that the flow is statistically stationary, and (iii) evaluate the contribution of each loss source. According to Hughues and Brighton,[35] losses can be estimated by accounting for the rise of entropy due to irreversible processes. Considering a control volume embedding the whole turbulent boundary layer within two given streamwise locations, the rate of entropy change is calculated as

$$\frac{\partial}{\partial t}\int_V \rho s \mathrm{d}V = \int_V \frac{(\tau\cdot\nabla)\mathbf{U}}{T}\mathrm{d}V - \int_S \rho s\mathbf{U}\cdot\mathrm{d}\mathbf{S} - \int_S \frac{\mathbf{q}}{T}\mathrm{d}\mathbf{S} + \int_V \frac{\mathbf{q}\cdot\mathbf{q}}{kT^2}\mathrm{d}V, \tag{7}$$

where V and S denote the control volume and the surfaces at its boundaries, respectively, ρ is the density, s is the entropy per unit mass, $\mathbf{U}$ is the velocity vector, T is the temperature, $\mathbf{q}$ is the energy transfer as heat, τ is the shear stress tensor, and k is the thermal conductivity of the fluid. By integrating Eq. (7) over a time span large enough to obtain the statistically stationary flow, one obtains[36]

$$\int_V \overline{\theta}\mathrm{d}V = \int_S \overline{\rho s\mathbf{U}}\cdot\mathrm{d}\mathbf{S} + \int_S \overline{\left(\frac{\mathbf{q}}{T}\right)}\cdot\mathrm{d}\mathbf{S}, \tag{8}$$

where the overline denotes the time-averaged quantities. The two terms on the right-hand side describe the time-averaged fluxes of entropy and the reversible entropy generation due to heat transfer across the control volume surfaces, respectively. The overall dissipation is $\overline{\theta}$, which can be rewritten as

$$\overline{\theta} = \overline{\frac{\Phi}{T}} + \overline{\frac{\varepsilon}{T}} + \overline{\frac{\zeta}{T}}. \tag{9}$$

The first two terms on the right-hand side, i.e., $\overline{\Phi/T + \varepsilon/T}$, account for the viscous dissipation, which can be further split into contributions due to the time-mean strain field, $\overline{\Phi/T}$, and the unsteady effects, i.e., the turbulent kinetic energy dissipation, $\overline{\varepsilon/T}$. The third term on the right-hand side, $\overline{\zeta/T}$, is the contribution to the irreversible entropy generation due to heat transfer between the fluid molecules.

B. Loss breakdown and dissipation coefficient via numerical computations

1. Direct numerical simulations

The procedure to calculate the three loss contributions to the overall dissipation using the results obtained from a DNS is exemplified in the following. The time-dependent dissipation term, i.e., the sum $\Phi/T + \varepsilon/T$, and the irreversible heat transfer term, ζ/T, are calculated at each simulation time step. During the post-process, the time average of these terms, i.e., $\overline{\Phi/T + \varepsilon/T}$ and $\overline{\zeta/T}$, can be computed knowing the time span of the simulation. From the Favre-averaged flow field, it is also possible to calculate the contribution due to the time-mean strain, $\overline{\Phi/T}$, which can then be subtracted from $\overline{\Phi/T + \varepsilon/T}$ to obtain the contribution due to turbulent dissipation, $\overline{\varepsilon/T}$. Alternatively, for a boundary layer in equilibrium, the integral of $\overline{\Phi/T}$ across the boundary layer thickness at a given streamwise location can be obtained by subtracting the integral of $\overline{\zeta/T}$ across the boundary layer thickness and the time-averaged turbulence production $\overline{P}$, defined as

$$\overline{P} = -\frac{1}{\rho_e U_e^3}\int_0^\delta \overline{\rho u_i' u_j'}\frac{\partial u_i}{\partial x_j}\mathrm{d}y, \tag{10}$$

from the entropy flux, calculated using the first term on the right-hand side of Eq. (8). In Eq. (10), the subscript e denotes the free stream quantities. For an equilibrium boundary layer, the production term $\overline{P}$ is equal to the turbulence dissipation, $\overline{\varepsilon}$. The approach just described is used in this study because the integration of the turbulence production is less sensitive to mesh size than that of $\overline{\varepsilon/T}$.

The turbulence production is also used to compute the dissipation coefficient that, for a compressible flow case, can be written as

$$C_\mathrm{d} = \overline{P} + \frac{1}{\rho_e U_e^3}\int_0^\delta \mu\left(\frac{\partial u_i}{\partial x_j}\right)^2 \mathrm{d}y, \tag{11}$$

where μ is the fluid dynamic viscosity. The first term in Eq. (11) is the contribution to the dissipation due to the turbulent production, while

the second one is the contribution due to the time-mean strain field. The dissipation coefficient here defined takes into account the dissipation of the mechanical energy of the mean flow rather than that of the total mechanical energy, in agreement with the approach used to compute dissipation coefficients with conventional Reynolds-averaged Navier–Stokes solvers.

2. Reduced-order modeling

Assuming a two-dimensional and stationary, turbulent flow, the resulting set of boundary layer flow equations can be solved numerically via reduced-order modeling.

Using Cebeci's approach,[37,38] the boundary layer equations can be transformed in a third-order partial-differential system of equations by using the so-called compressible Falkner–Skan transformation. To obtain the transformed equations, the coordinate transformation $(x, y) \rightarrow (x, \eta)$ is introduced, as well as the stream function ψ. Such scaling quantities are defined as

$$\eta = \sqrt{\frac{U_e}{\mu_e \rho_e x}} \int \rho \mathrm{d}y, \tag{12}$$

$$\psi(x, y) = \sqrt{\rho_e \mu_e U_e x} f(x, \eta), \tag{13}$$

where $f(x, \eta)$ is the integral of the normalized axial velocity component $u(x, \eta)/U_e$, the subscript e denotes the free stream conditions, and U is the magnitude of the velocity vector of the Cartesian components u and v. Identifying with the superscript $'$ the derivative with respect to η, the resulting momentum and energy equations for a two-dimensional steady-state boundary layer flow read, respectively,

$$(bf'')' + m_1 f f'' + m_2 \left[c - (f')^2\right] = x\left(f' \frac{\partial f'}{\partial x} - f'' \frac{\partial f}{\partial x}\right), \tag{14}$$

$$(eg' + df'f'')' + m_1 f g' = x\left(f' \frac{\partial g}{\partial x} - g' \frac{\partial f}{\partial x}\right), \tag{15}$$

with

$$f'' = \tilde{v}, \tag{16}$$

$$f' = \tilde{u}, \tag{17}$$

$$g' = \tilde{p}, \tag{18}$$

where $\tilde{u} = u/U_e$, $g = h_t/h_{t,e}$. $\tilde{v}$ and $\tilde{p}$ denote the derivatives of f' and g, respectively. Appendix A reports the definition of all the coefficients in Eqs. (14) and (15). The system of equations is valid for both laminar and turbulent regimes, but in the case of the turbulent flow, it requires the definition of an eddy viscosity model. For incompressible zero-pressure-gradient laminar boundary layer flows, the solution $f(x, \eta)$ is self-similar; therefore, the terms on the right-hand side of Eqs. (14) and (15) are equal to zero. This is not the case for turbulent flows because both the eddy viscosity ν_T and the turbulent Prandtl number Pr_T vary with the Reynolds number. For an adiabatic zero-pressure gradient boundary layer, i.e., $m_1 = m_2 = 0$, the boundary conditions in transformed variables read

$$f = 0, \quad f' = 0 \quad g' = 0 \quad \text{at} \quad \eta = 0, \tag{19}$$

$$f' = 1, \quad g = 1 \quad \text{at} \quad \eta = \eta_e, \tag{20}$$

which implies that, at the wall, there is no mass transfer across the surface, the no slip-condition is ensured, i.e., $u(y = 0) = 0$, and no energy is transferred from the wall to the fluid. At the boundary layer edge, instead, the speed and the total enthalpy values are equal to those of the free stream. The main advantage of using the Falkner–Skan coordinate transformation is that the velocity profiles weakly depend on the value of the free-stream Mach number. Therefore, the growth of the boundary layer thickness along the x coordinate is limited, and, from a computational perspective, a numerical solver would only require small adaptations of the mesh across the wall-normal direction. Moreover, the dependence of the solution on the x coordinate vanishes for the laminar regime, although it still affects the solution for the turbulent regime.

It is also possible to compute the overall dissipation in the boundary layer using transformed coordinates. The rate of entropy generation is computed by integrating the local entropy generation across the boundary layer thickness[1] and reads

$$\dot{S} = \int_0^\delta \frac{\tau_{xy}}{T} \frac{\partial u}{\partial y} \mathrm{d}y = \sqrt{\frac{\rho_e \mu_e}{x}} U_e^{\frac{5}{2}} \int_0^{\eta_e} \frac{CR}{T} \tilde{\nu}^2 \mathrm{d}\eta, \tag{21}$$

where τ_{xy} denotes the local shear stress. For turbulent flows, both τ_{xy} and CR include the contribution of the eddy viscosity whose value has to be estimated by means of a turbulence model. $\dot{S}$ can then be normalized to obtain the dissipation coefficient, defined in Eq. (1).

III. METHODOLOGY

A. DNS setup

To accurately evaluate the loss breakdown of a boundary layer flow, direct numerical simulations of zero-pressure gradient boundary layer flows of air and siloxane MM were performed. Table I lists the main properties of both fluids, together with those of other fluids whose related investigation is reported in Sec. IV B. The simulations were performed using *3DNS*,[36] a multiblock structured compressible Navier–Stokes solver for high-performance computations. The code can handle multiblock computations, with parallelization of the computational resources within each block. Spatial discretization is achieved with a fourth-order dispersion relation preserving (DRP) the finite difference central scheme[40] coupled with an eighth-order standard filter. Explicit time stepping is implemented with a four-stage fractional step Runge–Kutta method. Additionally, skew-symmetric splitting is used to stabilize the convective terms. Characteristic boundary conditions as described in Poinsot and Lele[41] are used to minimize the effect of reflecting pressure waves. The accuracy of the numerical model with respect to loss prediction has been assessed and is documented in previous works.[36,42,43]

TABLE I. Characteristic fluid properties of air, carbon dioxide,[39] isobutane, toluene, and siloxane MM.[33] γ_∞ is the specific heat ratio calculated in the dilute gas state.

	M_{mol} (kg/kmol)	T_{cr} (K)	p_{cr} (bar)	γ_∞	Γ_∞
Air	28.96	132.82	38.50	1.40	1.20
CO_2	44.01	304.13	73.77	1.29	1.13
Isobutane	58.12	407.81	36.29	1.08	1.04
Toluene	92.14	591.75	41.26	1.05	1.02
MM	162.3	518.70	19.31	1.03	1.01

TABLE II. Test cases evaluated in this study. Free-stream conditions and grid resolution parameters are reported. For all cases, the free-stream Mach number is set to 0.95. $H = \delta^*/\theta$ denotes the shape factor, $Re_\tau = \rho_w u_\tau \delta/\mu_w$ is the friction Reynolds number, and L_z/δ is the span-over-boundary layer thickness evaluated at the trailing edge.

	Fluid	$p_{r,e}$	$T_{r,e}$	Z_e	Ec_e	L_x (m)	H	Re_τ
Air	Air ideal gas	0.0264	2.182	1	0.36	0.023	1.84	390
iMM	Siloxane MM	0.1	1	0.96	$2.1 \cdot 10^{-2}$	$5 \cdot 10^{-3}$	1.45	385
niMM		1.15	1.05	0.54	$5.1 \cdot 10^{-3}$	$4.42 \cdot 10^{-4}$	1.49	378

	Fluid	x^+	$y^+_{1^{st}}$	$y^+_{10^{th}}$	z^+	$n_i \times n_j \times n_k$	L_z/δ
air	Air ideal gas	9.06	0.88	9.85	9.06	$2500 \times 800 \times 250$	4.5
iMM	Siloxane MM	9.13	0.88	9.85	9.13	$2500 \times 800 \times 250$	4.96
niMM		8.82	0.88	9.85	8.82	$2500 \times 800 \times 250$	5.13

Three different high-fidelity numerical simulations have been run. Table II lists the free stream conditions and the values of grid quality parameters for each test case. The values of the Eckert number in the free stream are also reported. All simulations have been performed by imposing a free-stream Mach number of 0.95. Inlet stagnation pressure and temperature and outlet static pressure values are prescribed at the boundaries. The values of the stagnation quantities are retrieved from the static ones reported in Table II and the value of the free-stream Mach number. The first case is a simulation of the boundary layer flow of air modeled as an ideal gas at standard conditions, i.e., $T_e = 288$ K and $p_e = 1$ bar. The *iMM* and *niMM* cases, instead, refer to simulations of siloxane MM flows whereby the free stream state is in dilute gas and dense vapor conditions, respectively. The thermodynamic states of the free stream characterizing the *iMM* and *niMM* are also shown in the temperature-entropy diagram of siloxane MM displayed in Fig. 1 The thermodynamic and transport properties of siloxane MM are calculated using entropy-based functional forms, which are explicit in density and internal energy, for both the equation of state and the constitutive law. This equation has been developed by fitting the values of compressibility factor, viscosity, and thermal conductivity obtained from accurate thermo-physical models[33] onto polynomial surfaces, according to the methodology described by Wheeler in Ref. 44.

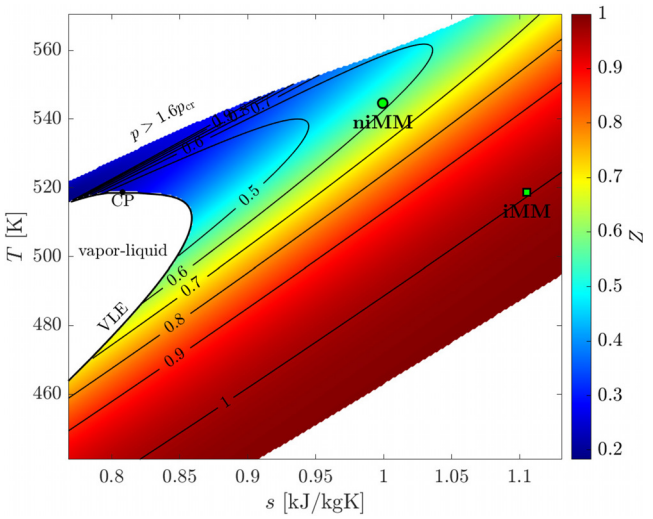

FIG. 1. Temperature-entropy diagram of siloxane MM. The black contour lines denote iso-γ_{pv} levels. The thermodynamic states of the free stream for the *iMM* and *niMM* cases presented in Table II are highlighted with green markers.

Figure 2 shows the computational grid used for the air case. The number of grid points in each direction, as well as the corresponding values of x^+, y^+ at the first cell in the wall proximity and z^+ are reported in Table II. According to the guidelines reported by Poggie *et al.*,[45] i.e., $10 \leq x^+ \leq 20$ and $5 \leq z^+ \leq 10$, the simulations performed in this study can be classified as DNS. Table III lists the characteristic cell lengths along x, y, and z in relation to the Kolmogorov length scale, defined as $\tilde{\eta} = [\bar{\mu}^3/(\bar{\rho}^3\bar{\varepsilon})]^{0.25}$. Both the values calculated in the wall proximity and of the boundary layer edge are listed in the table. As already pointed out by Sciacovelli *et al.*,[29,30] due to the

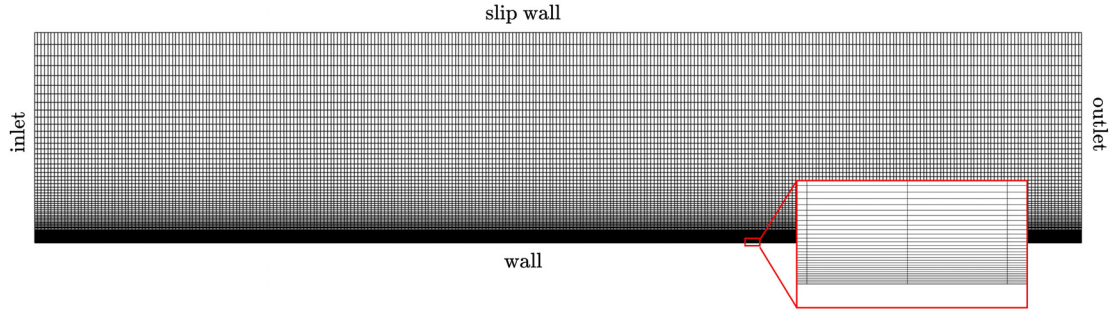

FIG. 2. Computational domain used to simulate the air case. To better visualize the mesh structure, only one every 8 grid line is shown along both the x and y coordinates. A detail of the near-wall grid is also displayed.

TABLE III. Grid resolution normalized with the Kolmogorov length scale $\tilde{\eta}$ for the cases listed in Table II. The resolution is evaluated at the wall (subscript w) and at the boundary layer edge (subscript e).

	$(\Delta x/\tilde{\eta})_w$	$(\Delta y/\tilde{\eta})_w$	$(\Delta z/\tilde{\eta})_w$	$(\Delta x/\tilde{\eta})_e$	$(\Delta y/\tilde{\eta})_e$	$(\Delta z/\tilde{\eta})_e$
Air	7.5	0.7	0.7	1.1	0.4	0.1
iMM	25.3	1.5	1.7	2.4	0.4	0.2
niMM	37.7	3	3.3	3.2	0.7	0.3

inherently large density and Reynolds number characterizing the flows of organic compounds, mesh resolution requirements are stricter than those needed to accurately simulate turbulent air flows. The characteristic cell length is much larger than the Kolmogorov length scale for the *iMM* and *niMM* cases. The largest values are those related to the *niMM* case due to the larger density of the fluid. The plate length is defined to ensure $Re_L = 5 \times 10^5$ at the outlet for all cases, where L is the plate length. To limit the amount of blockage and to ensure span-wise de-correlation, i.e., to allow all the turbulent structures to develop within the domain, the corresponding channel height and width are defined as 20% and 10% of the plate length, respectively. The prescribed height of the domain ensures that the influence of the blockage caused by the upper free-slip surface on the flow is negligible: the measured values of Clauser's beta parameter[46] at the boundary layer edge is defined as

$$\beta_{Cl} = \frac{\delta^*}{\tau_w}\frac{dp}{dx}, \tag{22}$$

where δ^* is the displacement thickness and are within the $-0.1 < \beta_{Cl} < 0$ range at $Re_\theta = 800$ for all the investigated cases. By using the definition of β_S proposed by Spalart and Watmuff,[47] i.e.,

$$\beta_S = \frac{\delta}{1/2\rho_e U_e^2}\frac{dp}{dx}, \tag{23}$$

the obtained range is $-0.4 < \beta_S \cdot 10^3 < 0$ at $Re_\theta = 800$, in line with the results by Wu and Moin.[16] Therefore, the mildly favorable pressure gradient induced by the presence of an upper wall has a negligible effect on the boundary layer flow. Stagnation temperature and pressure boundary conditions are prescribed at the inlet, and static pressure is instead prescribed at the outlet. No-slip adiabatic wall conditions are imposed at the wall. The upper surface is modeled as a free-slip wall, while periodic boundary conditions are imposed on the two side surfaces along the spanwise direction. To avoid numerical instability at the leading edge, a laminar self-similar profile of velocity and static enthalpy computed using the Blasius solution at $Re_x = 10^5$ is imposed at the inlet. The CFL number is one. No sub-scale modeling for the turbulence is applied.

To initialize the turbulent simulations, laminar two-dimensional computations using the boundary conditions listed in Table II were first performed. Then, three-dimensional laminar simulations were performed for the first 10 000 time steps, the two-dimensional solution being used to initialize the computation. After 10 000 time steps, transition to turbulence is promoted by introducing a body-force trip at a location x such that $Re_x = 2 \times 10^5$. A forcing term consisting of a square wave across the plate width, i.e., along the z-direction, is introduced in the momentum equation, i.e.,

$$\rho\mathbf{U} = \rho\mathbf{U}[1 - F_k(z)F(x,y)], \tag{24}$$

where k is the node index along the z direction. The forcing terms $F_k(z)$ and $F(x, y)$ are defined as

$$F(x,y) = e^{-S\left[(x-x_{trip})^2+(y-y_{trip})^2\right]}, \tag{25}$$

$$F_k(z) = \begin{cases} 1 & \text{if } \mathrm{mod}(k,12) < 6, \\ 0 & \text{if } \mathrm{mod}(k,12) \geq 6. \end{cases} \tag{26}$$

The forcing scale S is set equal to the local boundary layer thickness at the trip streamwise location. To enhance computational robustness, the trip is set to linearly grow from an amplitude of 0 to its maximum amplitude within 1000 iterations.

Statistical averages are performed over the span-wise direction and over at least two convective time units based on the free-stream velocity and the axial chord. During the simulations, the time-mean flow field and turbulence quantities are calculated using a Favre (density-weighted) time-averaging technique. In Appendix B, the accuracy of the solution for the air case is compared against well-established literature results for calorically perfect gases. The DNS simulations have been run on the Dutch national supercomputer Snellius.[48] Each simulation, consisting of 500×10^6 grid points, has been run on 30 nodes, each of them consisting of 128 AMD Rome 7H12 processors with a CPU speed of 2.6 GHz and 256 GiB memory per node. On average, each simulation has consumed 250 thousand core hours to run $\sim$ 400 k time steps.

B. Reduced-order model setup

The in-house boundary-layer Matlab code *BLnI*, in which the system of PDE described in Sec. II B 2 is discretized and numerically solved, is used to estimate the viscous dissipation in boundary layer flows of several compounds. The system of equations is solved numerically with the Keller–Box method.[37] First, the differential equations are converted into an equivalent first-order system of equations. The derivatives are then approximated using a centered finite difference scheme over a rectangular and nonuniform grid discretized in the $x - \eta$ plane. Newton's method is used to solve the resulting algebraic system of equations. The numerical scheme is unconditionally stable and is second-order accurate. Thermo-physical fluid properties are estimated using a well-known program.[34] Turbulent calculations are performed using the Cebeci–Smith turbulence model, where the eddy viscosity is modeled as a function of the velocity field, the density ratio $c = \rho_e/\rho$, the Chapman–Rubesin parameter $CR = (\rho U)/(\rho_e U_e)$, and the local Reynolds-number Re_x. Appendix C lists all the equations defining the Cebeci–Smith eddy viscosity and eddy conductivity models.

The same cases reported in Table II were computed with *BLnI* to verify the results by comparison with those obtained with DNS. Likewise, for the DNS, the transition is triggered at a streamwise location such that $Re_x = 2 \times 10^5$. The plate length over which the flow is in the turbulent regime also matches that of the high-fidelity numerical simulations.

In addition, to gain further insight into the influence of the fluid and nonideal thermodynamic effects on viscous dissipation, a systematic study was carried out. A second set of calculations was run for the fluids listed in Table I. For each fluid, several simulations using the boundary conditions listed in Table IV were run. Each pair of reduced

TABLE IV. Boundary conditions for the second set of simulations conducted with *BLnI*.

	$T_{r,e}$	$p_{r,e}$	M_e	$\gamma_{pv,e}$
$Z_e \sim 1$	1	0.1	0.01–1.8	0.99
$Z_e \sim 0.5$	1.05	1.15	0.01–1.8	0.60
$Z_e \sim 0.25$	1.01	1.1	0.01–1.8	1.40

temperature and pressure values fixes the free-stream thermodynamic state and, in turn, the values of the compressibility factor Z_e and of the isentropic exponent $\gamma_{pv,e}$. For each pair of $T_{r,e}$ and $p_{r,e}$, ten simulations at increasing values of the free-stream Mach number ranging between 0 and 1.8 were performed. The plate length was adapted to achieve $Re_L = 10^6$ for all simulations. The domain was discretized with a grid consisting of 150 points in the streamwise direction and 100 in the wall-normal direction. The first grid spacing in the normal-to-wall direction was set to 0.000 01 m, with a grid expansion factor of 1.02. These values were proven to ensure grid-independent results. The solver calculates the boundary layer flow variables at each streamwise location, from inlet to outlet. If needed, the mesh size along the wall-normal η direction is automatically adapted to account for the growth of the boundary layer. Adiabatic conditions are imposed on the wall.

IV. RESULTS

A. Dissipation analysis by means of DNS

Figure 3 shows the results of the loss breakdown analysis based on the approach described in Sec. II A for the cases listed in Table II. To avoid nonphysical results due to the presence of the transition trip, the entropy fluxes [Eq. (8)], the overall turbulence production $\overline{P}$ [Eq. (10)], and the values of both the dissipation due to the time-mean strain field $\overline{\Phi/T}$ and irreversible heat transfer $\overline{\zeta/T}$ [Eq. (9)] have been computed by integrating over a control volume encompassing the equilibrium region up to the streamwise location x, which is considered for the loss breakdown evaluation. For all the cases, the inlet boundary of the control volume is located after the transition point at $x/L \sim 0.35$ ($Re_\theta \sim 500$ at this location). The values of the shape factor H in the equilibrium region are nearly constant for all the cases under investigation, i.e., the flow is in equilibrium: Table II lists their values. Figure 4 shows the loss breakdown at a streamwise location corresponding to $Re_\theta \simeq 850$ to better appreciate the quantitative differences among the three cases. The percentage of the contribution of each loss source in relation to the total dissipation is also reported.

Overall, the *iMM* and *niMM* cases are characterized by a larger total dissipation at fixed Re_θ than the air case. Moreover, the boundary layer flow of siloxane MM at $Z_e \sim 1$ is more dissipative than that of the same fluid in thermodynamic conditions for which $Z_e \sim 0.5$. Concerning the breakdown of each loss source, the contribution of the turbulence dissipation is quantitatively similar for all three cases, the *iMM* case featuring the lowest share ($\sim$56%). The contribution due to irreversible heat transfer is negligible in the *iMM* and *niMM* cases. In the air case, such a contribution becomes relevant ($\sim$6%) and the one due to the time-mean strain field reduces by $\sim$7% in comparison to the values obtained for the two MM cases. This result can be explained as follows: in perfect gases of fluids made of simple molecules, the heat generated by the dissipation of the turbulent kinetic energy at small

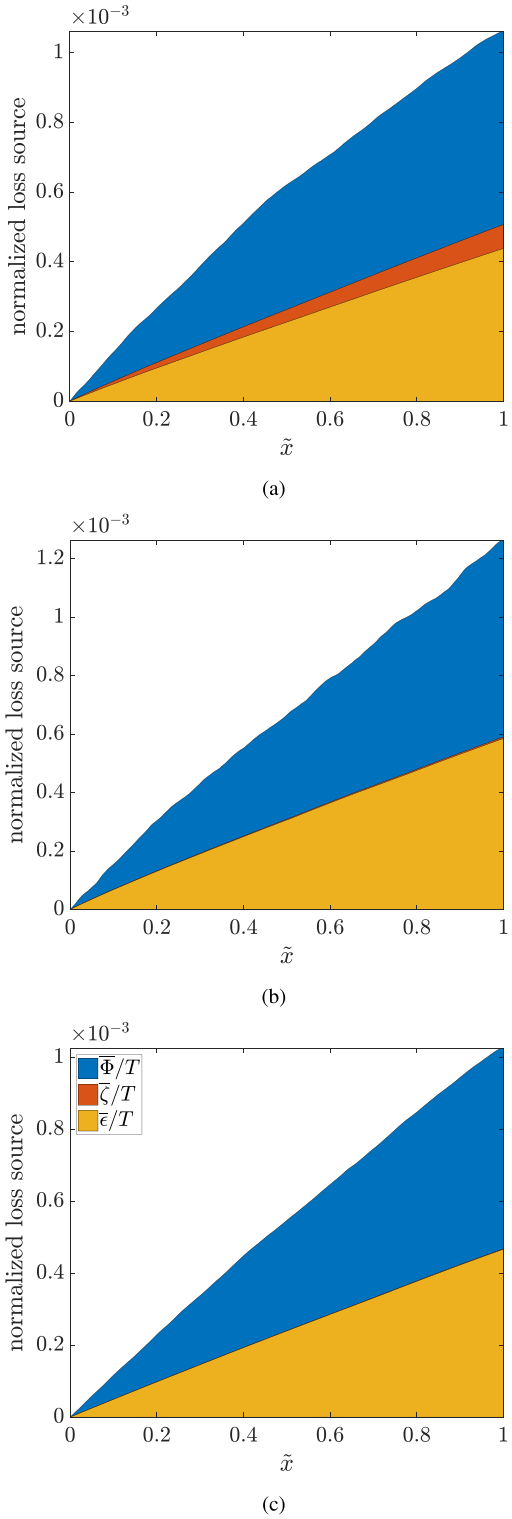

FIG. 3. Dissipation breakdown along the flat plate for the cases (a) air, (b) *iMM*, and (c) *niMM*. The integration of each contribution is performed from $\tilde{x} = 0$ to $\tilde{x} = 1$, where $\tilde{x} = (x - x_{tr})/(L - x_{tr})$. Each loss is normalized by $\rho_e U_e^3 L/T_e$.

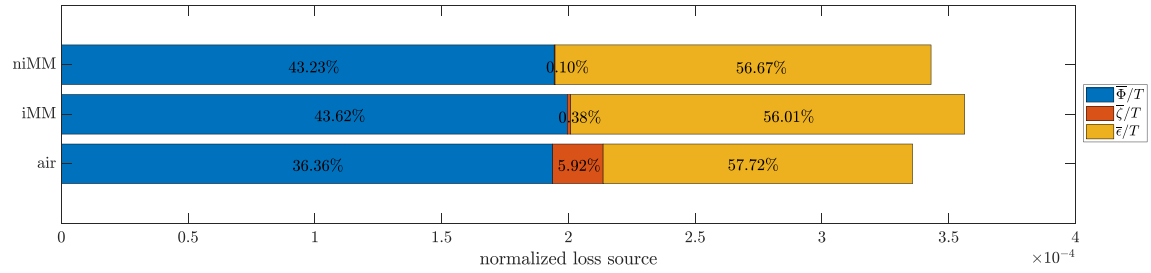

FIG. 4. Dissipation breakdown evaluated at a streamwise location corresponding to $Re_\theta \simeq 800$ for the cases listed in Table II. Percentages for each dissipation source are also reported.

scales induces variations of temperature larger than those occurring in fluids characterized by high molecular complexity, such as siloxane MM. In particular, the boundary layer flows of compounds characterized by high molecular complexity exhibit small temperature variations across the shear layer, thus limiting the diffusion of energy as heat among contiguous flow streams.

Figure 5 shows the variation of both the friction [Fig. 5(a)] and the dissipation coefficients [Fig. 5(b)] as a function of Re_θ for the cases of Table II. The results of the calculations conducted with *BLnI* are also displayed. Trends obtained from the DNS in the proximity of the tripping point are not reported due to nonphysical phenomena resulting from the simulation. The graphs show that the variations of both coefficients calculated from the DNS results qualitatively match those predicted by the reduced-order model. However, at fixed Re_θ, both C_f and C_d values estimated with *BLnI* do not match those obtained from the DNS results: for the air case, the maximum deviation is $\sim$5% on C_f and $\sim$10% on C_d.

Among the three cases under scrutiny, the lowest C_d value is found for the air case. This finding suggests that flows of fluids made of simple molecules are characterized by lower values of dissipation at fixed M_e and Re_θ. This trend can be explained by inspecting the value of the free stream Eckert number (see Table II), which is inherently lower in the case of dense vapor flows. In fluids made of complex molecules in both the ideal and the nonideal thermodynamic states, the thermodynamic and kinematic fields are decoupled even at free stream conditions for which the flow is highly compressible, and in terms of dissipation mechanisms, the physical behavior resembles that of an incompressible flow boundary layer.[10,29] This result is in agreement with those obtained by Pini and de Servi[22] for adiabatic laminar boundary layers of dense vapors at $M_e = 2$.

Figure 6 shows a comparison between the $C_f - Re_\theta$ [Fig. 6(a)] and the $C_d - Re_\theta$ [Fig. 6(b)] curves obtained from DNS and those obtained using the correlations by Drela and Giles.[14] Such correlations take into account the effect of flow compressibility by introducing a corrective coefficient that depends on both the shape factor and the free-stream Mach number. In Fig. 6(b), the $C_d - Re_\theta$ trend calculated using the empirical correlation by Denron[1] and Schlichting and Gersten[13] under the assumption of the turbulent incompressible flow is also plotted. This correlation reads

$$C_{d,Sc} = 0.0056 Re_\theta^{-\frac{1}{6}}. \tag{27}$$

Although predicting quite accurately the value of both C_f and C_d for air, Drela and Giles' correlations provide inaccurate results for the

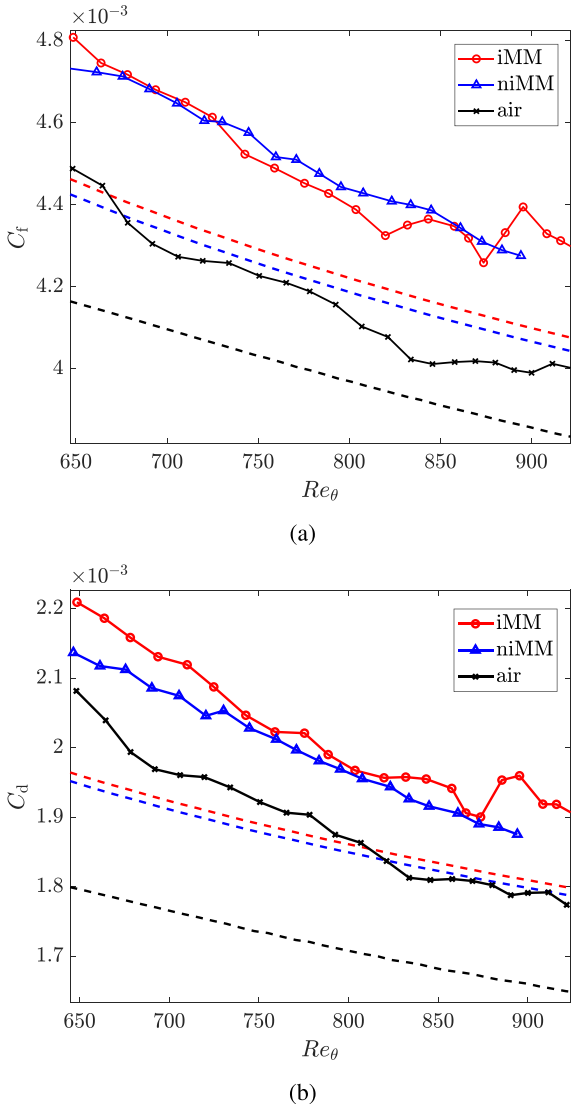

FIG. 5. (a) Skin friction coefficient vs Re_θ and (b) the dissipation coefficient vs Re_θ for all the cases of Table II. Results from DNS and turbulent simulations conducted with *BLnI* are plotted in solid and dashed lines, respectively.

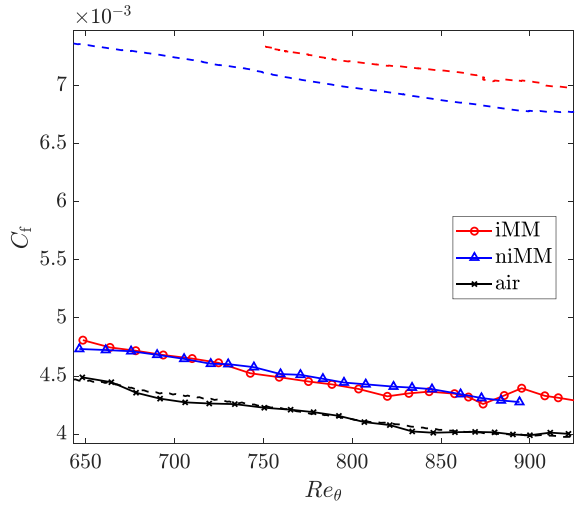

(a)

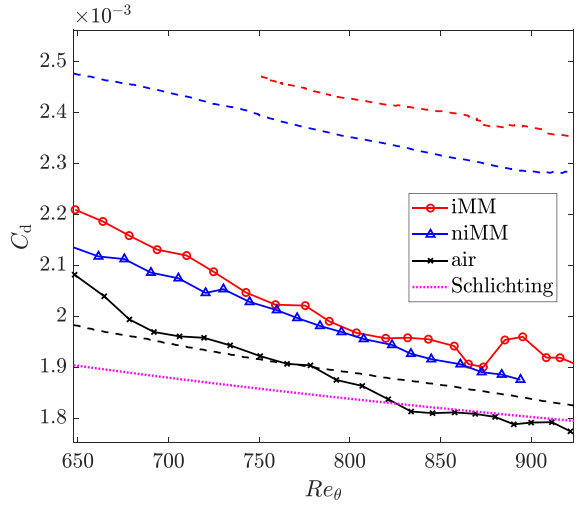

(b)

FIG. 6. (a) Skin friction coefficient vs Re_θ and (b) dissipation coefficient vs Re_θ for all the cases of Table II. Relations obtained with empirical correlations are also plotted for comparison. The dashed lines report the C_f vs Re_θ and the C_d vs Re_θ functions computed with the correlation by Drela and Giles.[14] The magenta line in figure (b) denotes the $C_d - Re_\theta$ function obtained using the Schlichting correlation.

iMM and *niMM* cases: for the *niMM* case, the predicted C_f and C_d values at fixed Re_θ are up to $\sim$ 30% larger than those obtained from DNS results. In the turbulent regime, the variation of C_d is similar to that predicted by the incompressible Schlichting correlation for the air case in the proximity of the plate trailing edge, while an offset ($\sim$ 7%) is observed for the other two cases. Such correlations have been validated only for transonic low-Reynolds number flows of air and do not take into account the effect of the fluid molecular complexity and the strong variations in the thermophysical properties characterizing dense organic vapors. According to Schlichting, for a zero-pressure gradient boundary layer flow in equilibrium, the relation between the dissipation and the skin friction coefficient is

$$C_d = \frac{C_f}{2}\frac{H^*}{2}, \tag{28}$$

where $H^* = \theta^*/\theta$ is the energy shape factor, and θ^* and θ being the kinetic energy and the momentum thicknesses, respectively. In the turbulent flow region, $H^* \sim 1.774$ for all cases, which is in line with the value computed by Jardine.[49] As a consequence, changes in the dissipation coefficient between the three cases are solely due to changes in the value of the skin friction coefficient.

B. Dissipation analysis through ROM

Figure 7 shows the variation of the dissipation coefficient C_d with Re_θ for flows of the fluids reported in Table I and the thermodynamic states listed in Table IV. The results have been calculated with *BLnI* assuming a fully turbulent flow and refer to boundary layer flows with $M_e = 1.4$. The $C_d - Re_\theta$ trend obtained with the correlation by Schlichting [Eq. (27)] valid for incompressible flows of air has also been plotted. Results for air obtained using the perfect gas equation of state are also displayed.

Regardless of the thermodynamic state, at a fixed Re_θ, C_d values are lower for boundary layer flows of fluids made of simple molecules than for those of complex organic compounds. This is due to their large heat capacity, which results in a quasi-isothermal temperature profile within the boundary layer, as can also be observed in the DNS results. The decrease in the dissipation coefficient with the fluid molecular complexity is more pronounced at $Z_e \sim 0.25$, i.e., at states in the proximity of the critical point one, where thermophysical properties are largely varying. As can be inferred from Eq. (30), the value of the dissipation coefficient depends on two dimensionless quantities: the temperature ratio T/T_e and the Chapman–Rubesin parameter CR. Figures 8(a)–8(c) show the trend of these two parameters, together with that of the density ratio ρ/ρ_e [Fig. 8(b)] across the boundary layer thickness, for flows of CO_2 and siloxane MM. In both cases, if $Z_e \to 0$, the boundary layer becomes more isothermal due to the increase in the fluid heat capacity in the dense vapor region. However, larger density gradients across the boundary layer are observed [Fig. 8(b)], with respect to flows of fluids in the dilute gas state. The effect of decreasing density across the boundary layer prevails over the one due to the increase in the dynamic viscosity, whose value scales with the temperature. As a consequence, the value of the Chapman–Rubesin parameter decreases. Consequently, with reference to Eq. (30), all fluids exhibit a decrease in the C_d value if the fluid state approaches that of the critical point. In summary, for the investigated fluids, the lower the Z_e is, the larger the density variations across the boundary layer caused by friction heating are, and the lower the associated irreversible entropy generation becomes.

Finally, Fig. 9 shows the change of the ratio $C_d/C_{d,Sc}$ as a function of the free-stream Mach number at fixed $Re_\theta = 10^3$ for all the fluids listed in Table I. It can be observed that $C_d/C_{d,Sc}$ approaches unity for compounds characterized by high molecular complexity in the dilute gas state and low M_e; conversely, it decreases with a decreasing molecular complexity, Z_e values, and increasing M_e values. The effect of compressibility, i.e., of the free-stream Mach number, is to enhance friction heating, which can sensibly change the velocity distribution across the boundary layer and reduce the wall skin friction coefficient, especially in fluids made of simple molecules and in the dilute gas state.

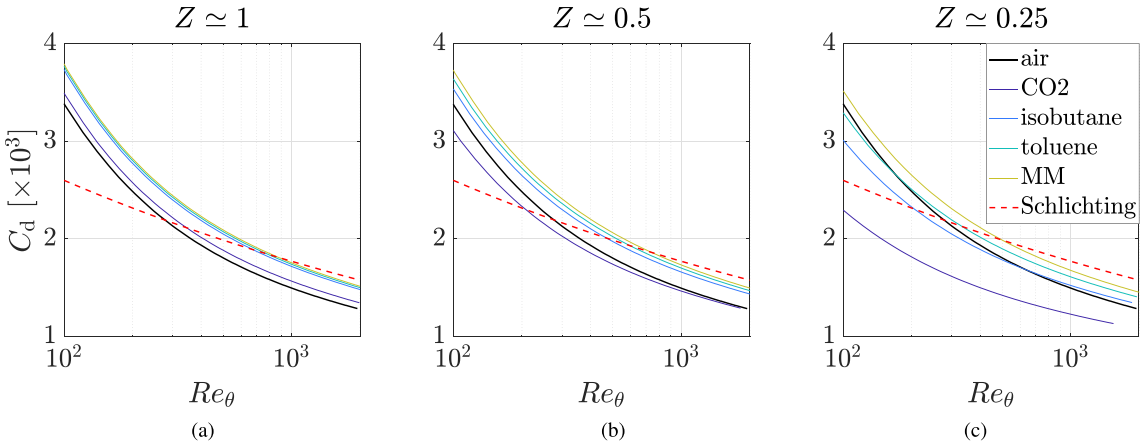

FIG. 7. Dissipation coefficient vs Re_θ for the fluids of Table I at $M_e = 1.4$. Data for air have been obtained assuming a calorically perfect gas. For comparison, trends evaluated with the Schlichting correlation are also reported.

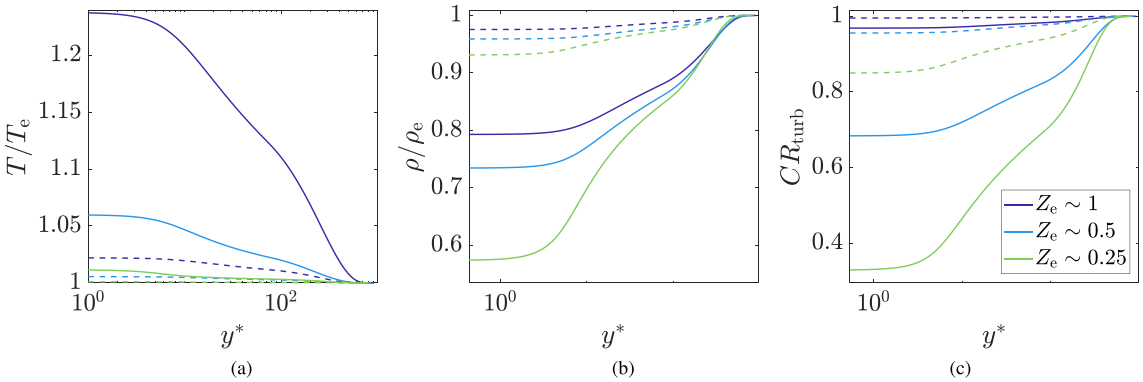

FIG. 8. Normalized (a) temperature, (b) density, and (c) turbulent Chapman–Rubesin parameter profiles across the boundary layer thickness as a function of y^* for carbon dioxide and siloxane MM and three different free-stream Z_e values. Continuous line denotes flows of CO_2, dashed line those of siloxane MM.

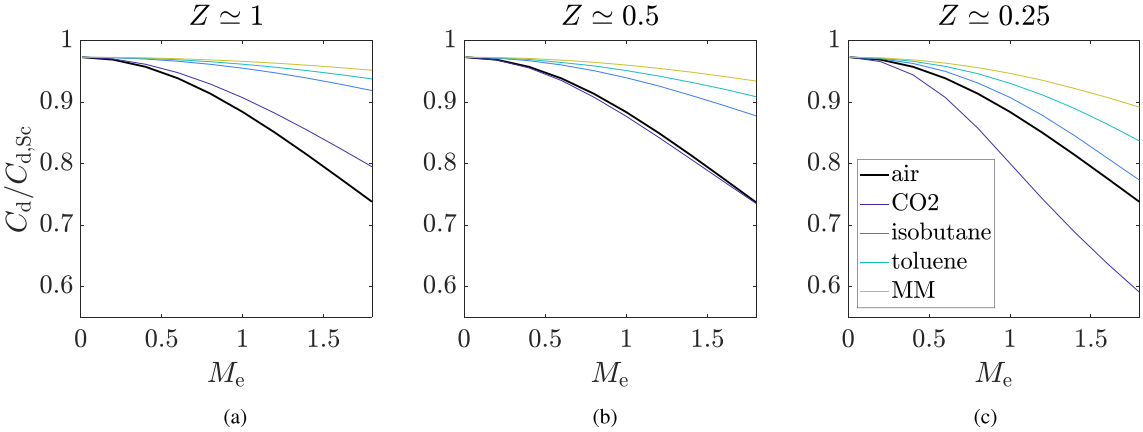

FIG. 9. Variation of the dissipation coefficient C_d with the free-stream Mach number M_e for several fluids in the turbulent regime. Three different free-stream thermodynamic states are analyzed: (a) $Z_e \sim 1$, (b) $Z_e \sim 0.5$, and (c) $Z_e \sim 0.25$. Data for air have been obtained assuming a calorically perfect gas. The dissipation coefficient has been normalized with the C_d value calculated using the Schlichting correlation.

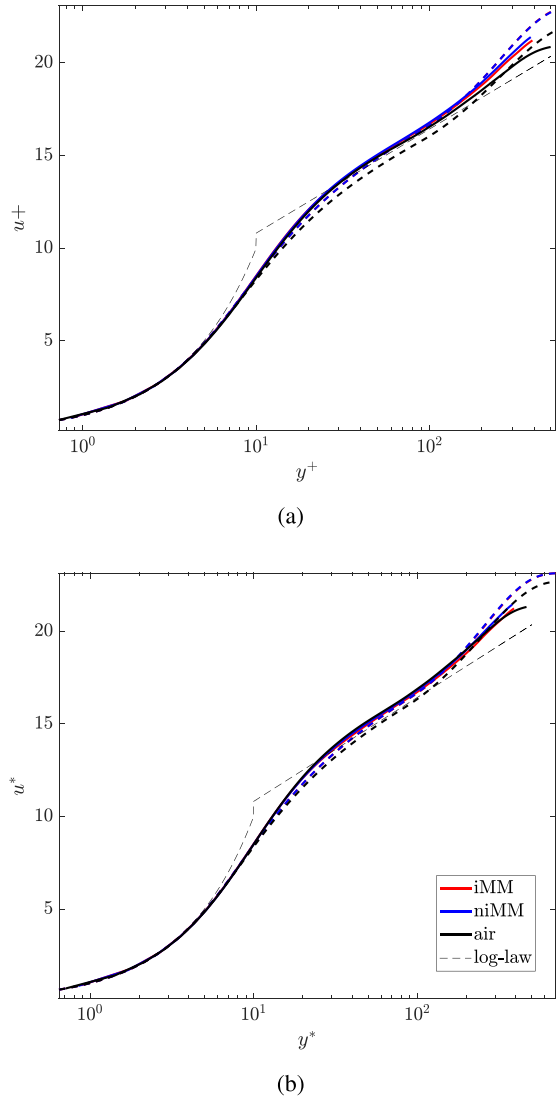

FIG. 10. Velocity profiles in (a) wall coordinates and (b) van Driest transformed coordinates. Continuous lines denote the values obtained with DNS, whereas dotted ones denote those obtained with the *BLnI* code. Black dashed lines indicate the linear and logarithmic laws, with $k = 0.41$ and $C = 5.2$.

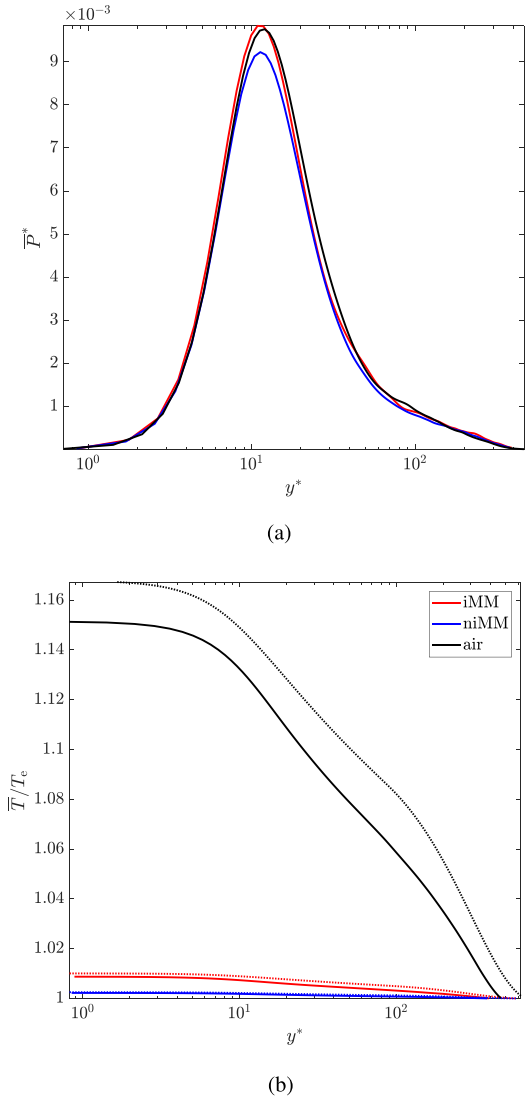

FIG. 11. (a) Normalized turbulence production $\overline{P}^* = \overline{P} \cdot \delta/(\rho_e U_e^3)$ vs y^+ and (b) temperature profiles for all the cases listed in Table II. Continuous lines correspond to the values obtained with DNS, whereas dotted ones indicate those obtained with the ROM. The trends have been evaluated at a location where $Re_\theta = 800$.

C. Flow field analysis

Figure 10(a) shows the velocity profiles in wall units, while Fig. 10(b) depicts the compressible van Driest velocity profile as a function of $y^* = \rho y u_\tau^*/\mu$, $u_\tau^* = \sqrt{\tau_w/\rho}$ and τ_w being the shear stress at the wall. Both profiles are evaluated at a location such that $Re_\theta = 800$. For a compressible boundary layer flow, the van Driest scaling reads

$$u^* = \frac{1}{\sqrt{\tau_w/\rho}} \int_0^{u_e} \sqrt{\frac{\rho}{\rho_w}} \mathrm{d}u. \tag{29}$$

Results obtained with *BLnI* for the same Re_θ are also reported. Regardless of the adopted scaling, no major deviations from the analytical law of the wall are observed for all cases in the viscous sublayer and in the buffer zone, where the peak in the turbulence production is observed, see Fig. 11(a). However, in the logarithmic region, the values obtained with the ROM do not fully overlap those obtained with the DNS in the air case. With respect to the velocity profiles obtained with the classical wall scaling [Fig. 10(b)], an $\sim 3\%$ difference between the u^+ values evaluated with the DNS and those evaluated with the ROM is observed at $y^+ = 40$. If a van Driest scaling $u*+(y*+)$ is used, all profiles collapse to the same trend and deviations from the log-law are less pronounced.

Figure 11(a) shows the turbulence production across the boundary layer thickness at a location such that $Re_\theta = 800$ for all the cases listed in Table II. The turbulence production peaks at $y^+ \sim 10$ in all

the cases. The peak is slightly more pronounced in the air and *iMM* case, while the *niMM* case exhibits the lowest maximum value of the normalized turbulent production. However, the differences are minimal and are arguably due to numerical dispersion.

Figure 11(b) displays the temperature profiles across the boundary layer evaluated at an x location corresponding to $Re_\theta = 800$. Results obtained from both the DNS and *BLnI* are plotted. It can be observed that the temperature increase in the proximity of the wall strongly depends on both the fluid molecular complexity and the thermodynamic fluid state. In particular, the temperature difference between the wall and the free stream is maximum in the case of air, while the boundary layer of siloxane MM is nearly isothermal in both the investigated thermodynamic conditions. This finding is inherently related to the large heat capacity of the organic fluid, or, similarly, to its high number of molecular degrees of freedom, which enables the fluid molecule to store more thermal energy than that stored by a molecule characterized by a lower number of degrees of freedom. Among the three cases, the *niMM* case shows a near-constant temperature profile due to the larger heat capacity of siloxane MM in the dense vapor state. In agreement with the findings by Sciacovelli *et al.*,[30] boundary layer flows of organic fluids in the compressible flow regimes typical of turbomachinery ($M_e \sim 1$–2) can thus be considered isothermal and exhibit features comparable to those characterizing incompressible flows. Furthermore, the temperature profile strongly affects the value of the dissipation coefficient. Using the Falkner–Skan variable transformation, one can write, for a turbulent flow,

$$C_d = \frac{1}{\sqrt{Re_x}} \int_0^{\eta_e} CR \frac{T_e}{T} \tilde{\nu}^2 d\eta, \tag{30}$$

where CR here also takes into account the contribution due to the eddy viscosity. At a fixed Reynolds number, for an ideal gas, variations of T_e/T prevail over those of CR, thus leading to a reduction of the C_d value for simple fluid molecules in the compressible flow regime.

Figure 12 shows the plots of the time-averaged density, viscosity, and Chapman–Rubesin parameter across the boundary layer as a function of the semi-locally scaled wall coordinate y^* for the three cases of Table II at a streamwise location corresponding to $Re_\theta = 800$. Results of the transitional boundary layer flow simulations performed with *BLnI* are also indicated. The averaged density [Fig. 12(a)] monotonically increases from the wall toward the free stream for all the cases. However, density variations are much smaller in the *iMM* and *niMM* cases, the smallest variations being observed in the dilute gas case *iMM*. Moreover, for all the cases, the density profile resembles the velocity profile, see Fig. 10. In particular, a linear profile of $\overline{\rho}$ with y^* is observed for $y^* \lesssim 12$ and a logarithmic one for $y^* \lesssim 100$. These results slightly differ from those obtained by Sciacovelli *et al.*,[30] who calculated such values only in boundary layer flows of dense organic vapor, whereas density variations in air flows better correlate with temperature variations. This difference is arguably due to the large free-stream Mach number values ($M_e = 2.25$ and $M_e = 6$) selected by the authors. The wall friction heating to which supersonic and hypersonic air flows are subjected is larger than the one characterizing the flows investigated in this work, where $M_e = 0.95$: in particular, the wall-to-free-stream temperature ratio at $M_e = 6$ is 6.5, while at the Mach number ($M_e = 0.95$) chosen for this simulation is 1.16 [Fig. 11(b)]: thus, a larger influence of the temperature on the density field can be observed in hypersonic flows. Moreover, the temperature profile is

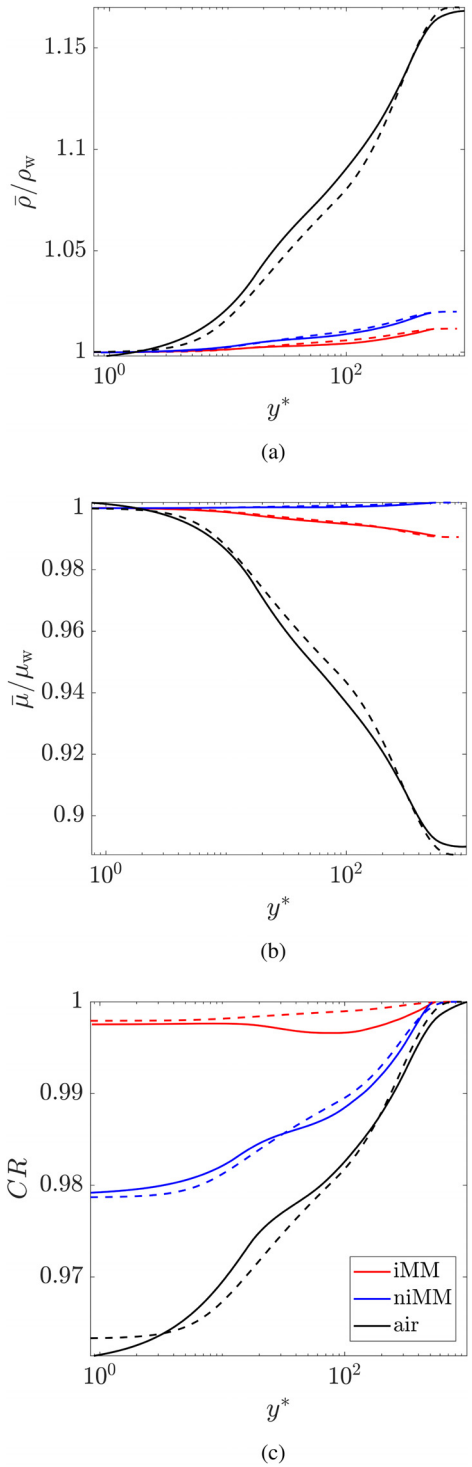

FIG. 12. Time-averaged (a) density, (b) dynamic viscosity, and (c) Chapman–Rubesin vs y^* for the cases listed in Table II. The statistics are normalized with the value of the corresponding variable evaluated at the wall. Continuous lines denote quantities evaluated using DNS; dashed lines, instead, those calculated with the *BLnI* code.

decoupled from the density profile in the *iMM* and *niMM* cases due to the larger number of molecular degrees of freedom and, consequently, the larger heat capacity characterizing these fluids, which, in turn, minimizes the friction heating at the wall.

The viscosity profile [Fig. 12(b)] qualitatively follows the profile of the temperature for the air and *iMM* cases, with a larger wall-to-free-stream ratio calculated for the air case. Conversely, the *niMM* case shows a liquid-like viscosity variation, i.e., the viscosity increases across the boundary layer, with a profile similar to that of the density. This effect has already been discussed in several other works.[29,30,50] However, the increase in viscosity across the boundary layer is here smaller than the one estimated by Sciacovelli *et al.* due to the use of a different and more accurate model for the transport properties of siloxane MM.[33] The local value of the Chapman–Rubesin parameter *CR* increases toward the free stream for all three cases [Fig. 12(c)]. Larger wall-to-free stream differences are observed in the air case ($CR_w \sim 0.96$ at the wall) than in the other two. It can also be noted that the *CR* value in the dilute gas case *iMM* does not sensibly depart from unity, whereas it exhibits a larger departure from unity in the dense vapor case, *niMM*. As opposed to the temperature profile [Fig. 11(b)], larger density variations are observed in the dense vapor case than in the dilute gas case due to the strong gradients of thermophysical properties characterizing fluid states in the proximity of the critical point. This variation strongly influences that of *CR*, which, in turn, influences the overall dissipation within the boundary layer, see Eq. (30). The influence of both the Chapman–Rubesin parameter and the dense vapor state on the dissipation coefficient is further discussed in Sec. IV B. Although a quantitative mismatch is observed, the values obtained with *BLnI* are qualitatively in agreement with those obtained from DNS for the density, the viscosity, and the Chapman–Rubesin parameter. As a consequence, the reduced-order model is deemed sufficiently accurate for carrying out systematic studies aimed at providing evaluations of integral boundary layer parameters such as the C_d in the laminar and turbulent flow regimes.

Figure 13 shows the variations of the root mean square of the velocity, density, and pressure fluctuations across the boundary layer for the three cases of Table II at a streamwise location corresponding to $Re_\theta = 800$. The turbulence intensity profiles [Fig. 13(a)] feature a similar variation in all three cases. Deviations are mainly observed in the outer region, i.e., $y^* > 300$, where both the *iMM* and *niMM* cases display a plateau at $y^* \sim 700$, whereas the air exhibits a plateau at $y^* > 10^3$. The same profile is also observed for the turbulence intensity (not shown), defined as $Tu = \sqrt{2/3k}/U_e^3$, where k is the turbulence kinetic energy, which also takes into account the intensity of the turbulent fluctuations in the y and z directions. The peak in the turbulence intensity occurs at $y^* \sim 12$, which corresponds to the location of maximum turbulence production. Conversely, the root mean square of the density fluctuations [Fig. 13(b)] reaches a maximum at $y^* \sim 30$ in all the investigated cases. The maximum in the root mean square of the pressure fluctuations, instead, is observed at $y^* \sim 20$. However, the peak is less pronounced in the cases in which siloxane MM is the working fluid. In particular, the relative deviation between the value of the density fluctuation at $y^* \sim 12$ and $y^* \sim 1$ is 21% for the *iMM* and 45% for the *niMM* cases, whereas this is much larger for the air case (530%). This is in line with what has been discussed about the time-average density, which shows larger variations across the boundary layer in the air case. Overall, regardless of the fluid and its

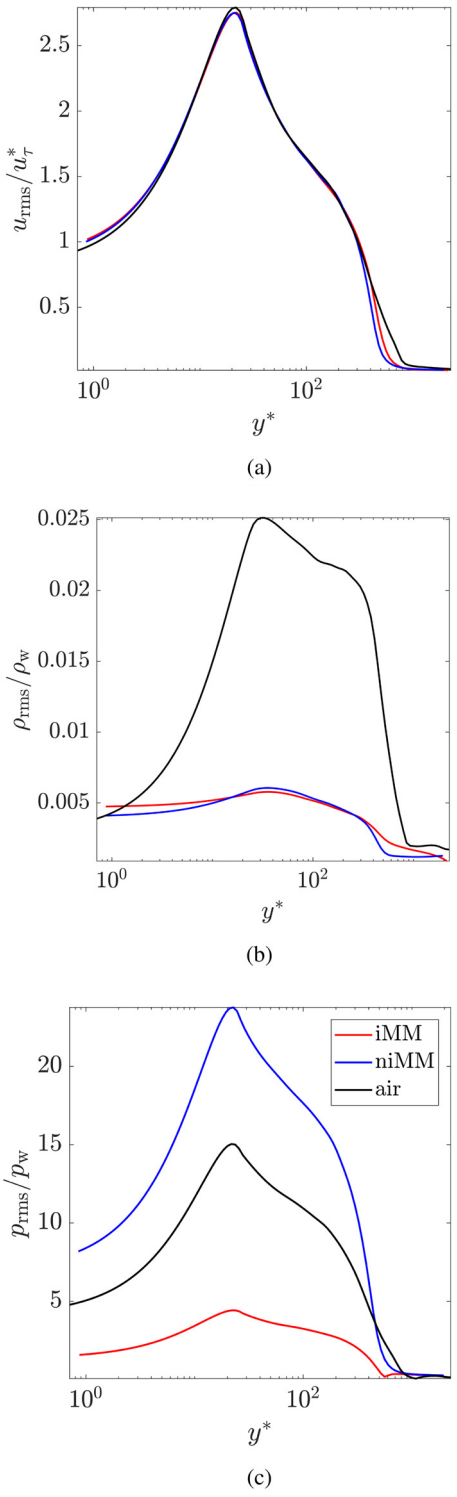

FIG. 13. Root mean square (a) streamwise velocity, (b) density, and (c) pressure fluctuations vs y^* for the cases listed in Table II. Velocity fluctuations are normalized with the semi-local friction velocity u_τ^*; see Eq. (29). Temperature and pressure fluctuations are normalized with the value of the corresponding variable evaluated at the wall.

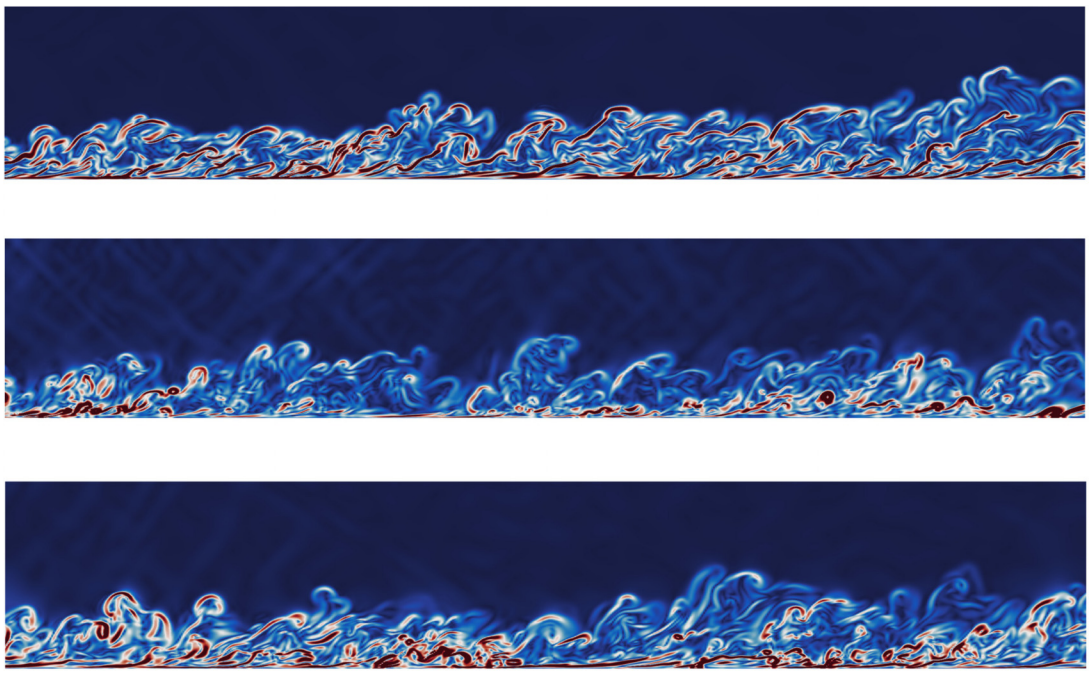

FIG. 14. Normalized density gradient ($\nabla\rho/(\overline{\rho}/L)$) within the equilibrium region at a streamwise coordinate corresponding to $Re_\theta \sim 800$. Snapshots taken after 150 k time steps for (a) air, (b) iMM, and (c) niMM.

thermodynamic state, Morkovin's hypothesis for which density fluctuations are negligible ($\rho_{\mathrm{rms}}/\overline{\rho}$) is satisfied, in agreement with the findings by Sciacovelli *et al.*

Finally, Fig. 14 shows the instantaneous snapshots of the magnitude of the density gradient $|\nabla\rho|$ for each case after 150k time steps. The density gradient is normalized by $\overline{\rho}/L$. Elongated, sheet-like flow structures corresponding to high-density gradients moving toward the boundary layer edge are observed in the air case. Conversely, high-density gradient structures are concentrated on the wall in both the *iMM* and *niMM* cases. This distribution is arguably due to the inherently larger density characterizing siloxane MM.

V. CONCLUSION

Direct numerical simulations of zero-pressure gradient boundary layer flows of air and siloxane MM with the fluid in both dilute gas and dense vapor thermodynamic states have been performed. All dissipation sources have been discerned and analyzed. The trend of both the skin friction and the dissipation coefficients as a function of the Reynolds number, as well as those of the velocity and temperature profiles, have been discussed and compared against those obtained from an in-house reduced-order model solving the two-dimensional turbulent boundary layer equations in transformed coordinates. Results from the reduced-order model have then been used to assess the influence of the fluid molecular complexity, the thermodynamic state, and the flow compressibility on the dissipation coefficient. Based on the results obtained from this work, the following conclusions can be drawn:

1. At fixed Reynolds number, the turbulent boundary layer flows of fluids made of complex molecules are characterized by a higher value of both the skin friction and the dissipation coefficient than flows of air. This is due to the decoupling between the thermal and the kinematic fields, as a consequence of the larger value of heat capacity of complex molecular fluids.
2. Regardless of the fluid thermodynamic state, turbulent boundary layer flows of complex molecules fluids can be assumed isothermal.
3. The contribution to the overall loss due to irreversible heat transfer is negligible in boundary layer flows of molecularly complex fluids, regardless of their thermodynamic state.
4. For a given fluid, at a fixed Reynolds number, the overall dissipation expressed in terms of the dissipation coefficient decreases if the state approaches that of the critical point. This is due to the large density gradients characterizing the flow across the shear layer, which leads to a decrease in the Chapman–Rubesin parameter value and, thus, of the dissipation coefficient.
5. In general, boundary layer flows of fluids made of simple molecules in the dense vapor state are less dissipative than those of complex organic compounds in the dilute gas state. This is due to the combined effects of the large density gradients characterizing states in the proximity of the critical point and the wall friction heating, which prevails in flows of fluids made of simple molecules.

Future works will investigate more in detail the structure of density and pressure fluctuations in ideal gas and dense vapor boundary layers. Flows of fluids other than air and siloxane MM will also be studied with the reduced-order model, as well as the effect of favorable and adverse pressure gradients. Analyses of the effect of the wall heat transfer in the boundary layer flow of organic fluids, as well as the

influence of the turbulence model, are also envisioned. The ultimate research goal is to develop an analytical model for the dissipation coefficient C_d as a function of the Reynolds number, the thermodynamic fluid state, the molecular complexity, the boundary layer shape factor, and the free-stream Mach number. Such a model can then be used to estimate the profile losses in internal flow devices such as turbomachinery or heat exchangers during the conceptual design phase.

ACKNOWLEDGMENTS

The authors acknowledge the contribution of Dr. Carlo De Servi, Dr. Adam J. Head, Dominic Dijkshoorn, and Federico Pizzi to the development and verification of *BLnI*. The contribution of Professor Dr. Piero Colonna to several interesting discussions on the physics of nonideal flows is also highly acknowledged. This research has been supported by the Applied and Engineering Sciences Domain (TTW) of the Dutch Organization for Scientific Research (NWO), Technology Program of the Ministry of Economic Affairs, Grant No. 15837.

AUTHOR DECLARATIONS

Conflict of Interest

The authors have no conflicts to disclose.

Author Contributions

Francesco Tosto: Conceptualization (equal); Formal analysis (lead); Methodology (equal); Software (lead); Supervision (lead); Writing – original draft (equal); Writing – review & editing (equal). **Andrew Wheeler:** Conceptualization (equal); Formal analysis (lead); Methodology (supporting); Software (supporting); Supervision (supporting); Writing – original draft (equal); Writing – review & editing (supporting). **Matteo Pini:** Conceptualization (equal); Formal analysis (lead); Methodology (equal); Software (lead); Supervision (lead); Writing – original draft (equal); Writing – review & editing (equal).

DATA AVAILABILITY

The data that support the findings of this study are available from the corresponding author upon reasonable request.

APPENDIX A: COEFFICIENTS FOR THE COMPRESSIBLE FALKNER–SKAN TRANSFORMED EQUATIONS

With reference to Eqs. (14) and (15), the coefficients for the compressible Falkner–Skan transformed boundary layer equations read as follows:

$$b = CR(1+\nu^+), \quad \nu^+ = \frac{\nu_T}{\nu}, \tag{A1}$$

$$c = \frac{\rho_e}{\rho}, \quad CR = \frac{\rho\mu}{\rho_e\mu_e}, \quad CR_e = \frac{\rho_e\mu_e}{\rho_0\mu_0}, \tag{A2}$$

$$d = \frac{CU_e^2}{h_{0,e}}\left[1 - \frac{1}{\mathrm{Pr}} + \nu^+\left(1 - \frac{1}{\mathrm{Pr}_T}\right)\right], \tag{A3}$$

$$e = \frac{C}{\mathrm{Pr}}\left(1 + \nu^+\frac{\mathrm{Pr}}{\mathrm{Pr}_T}\right), \tag{A4}$$

$$f' = \frac{u}{u_e}, \tag{A5}$$

$$g = \frac{h_0}{h_{0,e}}, \tag{A6}$$

$$m_1 = \frac{1}{2}[1 + m_2 + m_3] = \frac{1}{2}[1 + m_3 + m_4 + m_5], \tag{A7}$$

$$m_2 = \frac{x}{u_e}\frac{\mathrm{d}u_e}{\mathrm{d}x} = m_4 + m_5 = \frac{m_4}{1 + (\Gamma - 1)M_e^2}, \tag{A8}$$

$$m_3 = \frac{x}{C_e}\frac{\mathrm{d}C_e}{\mathrm{d}x}, \tag{A9}$$

$$m_4 = \frac{x}{M_e}\frac{\mathrm{d}M_e}{\mathrm{d}x}, \tag{A10}$$

$$m_5 = \frac{x}{c_e}\frac{\mathrm{d}c_e}{\mathrm{d}x}. \tag{A11}$$

In the equations, ν, ν_T, and c denote the kinematic viscosity of the fluid, the turbulent eddy viscosity, and the speed of sound.

APPENDIX B: VALIDATION OF THE DNS RESULTS FOR THE AIR CASE

The results obtained from the DNS for the air case are here compared with reference to high-fidelity simulations of zero-pressure gradient turbulent flows available in the literature. We here compared our results with those obtained by Wu and Moin[16] and Pirozzoli and Bernardini.[17] The first authors performed incompressible direct numerical simulations, the latter supersonic compressible DNS at $M_e = 2$.

Figures 15(a) and 15(b) show the velocity profiles obtained using the classical wall scaling and the van Driest scaling. With reference to Fig. 15(a), the profile obtained for the air case is in good agreement with the solution by Wu and Moin, the differences being mostly attributed to compressibility effects. Larger deviations in the logarithmic region are instead observed with the solution by Pirozzoli and Bernardini due to the high free-stream Mach number characterizing this simulation. A good agreement with the solution by Wu and Moin is instead observed when inspecting the van Driest scaled profile; see Fig. 15(b).

Figures 16(a)–16(c) show the Reynolds fluctuations in the streamwise, wall-normal, and spanwise directions. Maximum values of both v_{rms} and w_{rms} are lower than those obtained by Wu and Moin, with the maximum being shifted to lower y^+ values. Opposite considerations hold when compared with results by Pirozzoli and Bernardini. This is in line with the results by Wenzel *et al.*[18] who observed a decrease in the maxima of the fluctuations at fixed Re_τ and increasing values of the free-stream Mach number.

APPENDIX C: THE CEBECI–SMITH TURBULENCE MODEL

The Cebeci–Smith model[37] is an algebraic 0-equation eddy viscosity turbulence model. It models the eddy viscosity as a function of the turbulent velocity field, the density ratio $c = \rho_e/\rho$, the

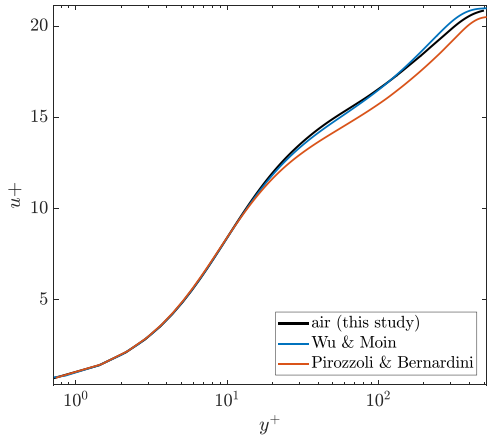

(a)

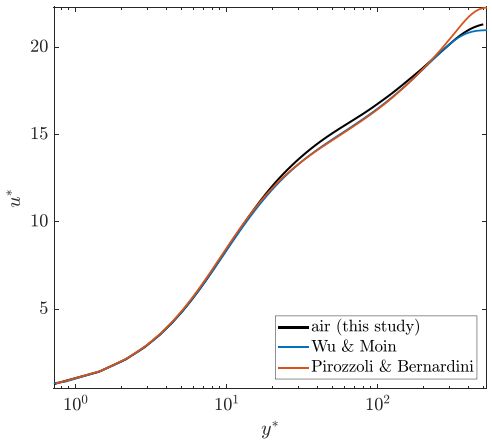

(b)

FIG. 15. Velocity profiles in (a) wall coordinates and (b) van Driest transformed coordinates for the air case at $Re_\theta = 900$. Profiles from Wu and Moin (incompressible, $Re_\theta = 900$) and Pirozzoli and Bernardini ($M_e = 2$, $Re_\tau = 450$) are also plotted.

Chapman–Rubesin parameter CR, and the Reynolds-number Re_x. The non-dimensional eddy viscosity $\nu^+ = \nu_T/\nu$ for the inner and outer layers reads

$$(\nu^+)_{\text{inner}} = \kappa^2 \frac{1}{C}\frac{1}{c^3}\sqrt{\text{Re}_x} I^2 v[1-\exp(-y/A)]^2 \gamma_{\text{tr}}\gamma, \quad 0 \le \eta \le \eta_c, \tag{C1}$$

$$(\nu^+)_{\text{outer}} = \alpha \frac{1}{C}\frac{1}{c^2}\sqrt{\text{Re}_x}\left[\int_0^{\eta_e} c(1-u)\,\mathrm{d}\eta\right]\gamma_{\text{tr}}\gamma, \quad \eta_c \le \eta \le \eta_e, \tag{C2}$$

where η_c is the location of the inner layer edge in transformed coordinates, and

$$y/A = \frac{N}{A^+} c^{-3/2}\frac{\sqrt{C_w}}{C}\text{Re}_x^{1/4} I v_w^{1/2}, \quad I = \int_0^{\eta} c\,\mathrm{d}\eta, \quad I_e = \int_0^{\eta_e} c\,\mathrm{d}\eta, \tag{C3}$$

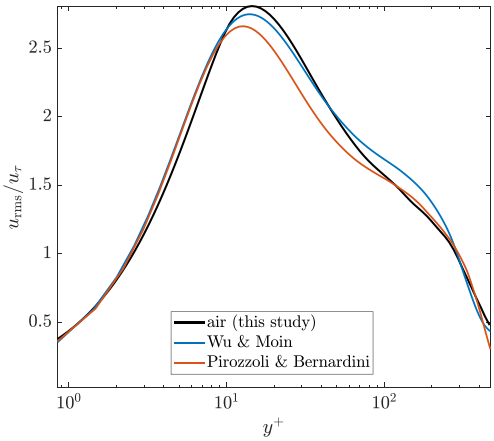

(a)

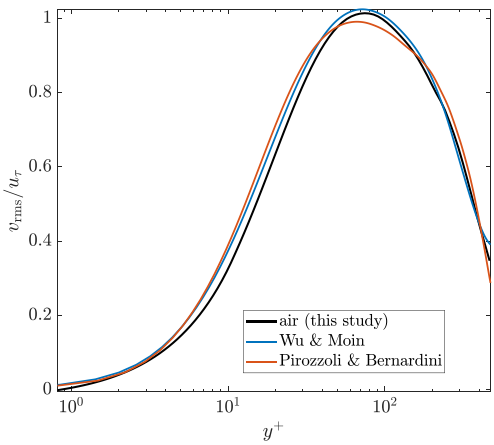

(b)

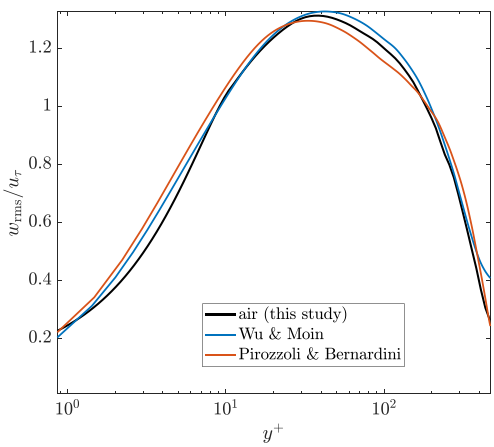

(c)

FIG. 16. Normalized components of the Reynolds fluctuations (a) u_{rms}, (b) v_{rms}, and (c) w_{rms} for the air case at $Re_\theta = 900$. Profiles from Wu and Moin (incompressible, $Re_\theta = 900$) and Pirozzoli and Bernardini ($M_e = 2$, $Re_\tau = 450$) are also plotted.

$$N^2 = 1 - 11.8 C_w c_w^3 p^+, \quad p^+ = \frac{m_2}{\mathrm{Re}_x^{1/4}} (C_w c_w \nu_w)^{-3/2}, \tag{C4}$$

$$\gamma = \left(1 + 5.5 (I/I_e)^6\right)^{-1}. \tag{C5}$$

The closure coefficients are set to

$$\kappa = 0.40, \quad A^+ = 26, \quad \alpha = 0.0168. \tag{C6}$$

For transitional boundary layers, the intermittency factor γ_{tr} reads

$$\gamma_{tr} = 1 - e^{\left(-G_{tr}(x - x_{tr}) \int_{x_{tr}}^{x} \frac{dx}{u_e}\right)}, \tag{C7}$$

with

$$G - \mathrm{tr} = 8.33 \cdot 10^4 \frac{U_e^3}{\nu_e} Re_x^{-1.34}. \tag{C8}$$

The turbulent Prandtl number Pr_T model reads

$$Pr_T = \frac{\kappa[1 - \exp(-y/A)]}{\kappa_h[1 - \exp(-y/B)]}, \tag{C9}$$

where

$$y/B = \frac{N}{B^+} c^{-3/2} \frac{\sqrt{C_w}}{C} \mathrm{Re}_x^{1/4} I \nu_w^{1/2}, \tag{C10}$$

$$B^+ = \frac{B^{++}}{Pr^{1/2}}, \tag{C11}$$

$$B^{++} = \sum_{i=1}^{5} C_i \left(\log_{10} Pr\right)^{i-1}, \tag{C12}$$

Pr being the Prandtl number, and the closure coefficients whose values are set to

$$\begin{aligned} \kappa_h = 0.44, \quad C_1 = 34.96, \quad C_2 = 28.79, \\ C_3 = 33.95, \quad C_4 = 6.33, \quad C_5 = -1.186. \end{aligned} \tag{C13}$$

REFERENCES

[1] J. D. Denton, "The *1993 IGTI scholar lecture*: Loss mechanisms in turbomachines," J. Turbomach. **115**, 621–656 (1993).
[2] S. Dixon and C. Hall, *Fluid Mechanics and Thermodynamics of Turbomachinery* (Elsevier Science, 2013).
[3] F. M. White and J. Majdalani, *Viscous Fluid Flow* (McGraw-Hill New York, 2006), Vol. 3.
[4] P. Colonna, E. Casati, C. Trapp, T. Mathijssen, J. Larjola, T. Turunen-Saaresti, and A. Uusitalo, "Organic Rankine cycle power systems: From the concept to current technology, applications, and an outlook to the future," J. Eng. Gas Turbines Power **137**, 100801 (2015).
[5] K. Brun, P. Friedman, and R. Dennis, *Fundamentals and Applications of Supercritical Carbon Dioxide (sCO2) Based Power Cycles* (Woodhead Publishing, 2017).
[6] K. Herold, R. Radermacher, and S. Klein, *Absorption Chillers and Heat Pumps* (Taylor & Francis, 1996).
[7] A. Giuffre, P. Colonna, and M. Pini, "The effect of size and working fluid on the multi-objective design of high-speed centrifugal compressors," Int. J. Refrig. **143**, 43–56 (2022).
[8] J. Schiffmann and D. Favrat, "Design, experimental investigation and multi-objective optimization of a small-scale radial compressor for heat pump applications," Energy **35**, 436–450 (2010).
[9] E. M. Greitzer, C. S. Tan, and M. B. Graf, *Internal Flow: Concepts and Applications* (Cambridge University Press, 2004).
[10] F. Tosto, C. Lettieri, M. Pini, and P. Colonna, "Dense-vapor effects in compressible internal flows," Phys. Fluids **33**, 086110 (2021).
[11] D. A. Kouremenos and K. A. Antonopoulos, "Isentropic exponents of real gases and application for the air at temperatures from 150 K to 450 K," Acta Mech. **65**, 81–99 (1987).
[12] F. Tosto, A. Giuffré, P. Colonna, and M. Pini, "Non-ideal effects in compressible swirling flows," in *Proceedings of the 3rd International Seminar on Non-Ideal Compressible Fluid Dynamics for Propulsion and Power*, edited by M. Pini, C. De Servi, A. Spinelli, F. di Mare, and A. Guardone (Springer International Publishing, Cham, 2021), Vol. 28, pp. 36–43.
[13] H. Schlichting and K. Gersten, *Boundary-Layer Theory*, 9th ed. (Springer, Berlin Heidelberg, New York, NY, 2016).
[14] M. Drela and M. B. Giles, "Viscous-inviscid analysis of transonic and low Reynolds number airfoils," AIAA J. **25**, 1347–1355 (1987).
[15] P. R. Spalart, "Direct simulation of a turbulent boundary layer up to $R_\theta = 1410$," J. Fluid Mech. **187**, 61–98 (1988).
[16] X. Wu and P. Moin, "Direct numerical simulation of turbulence in a nominally zero-pressure-gradient flat-plate boundary layer," J. Fluid Mech. **630**, 5–41 (2009).
[17] S. Pirozzoli and M. Bernardini, "Turbulence in supersonic boundary layers at moderate Reynolds number," J. Fluid Mech. **688**, 120–168 (2011).
[18] C. Wenzel, B. Selent, M. Kloker, and U. Rist, "DNS of compressible turbulent boundary layers and assessment of data/scaling-law quality," J. Fluid Mech. **842**, 428–468 (2018).
[19] P. A. Thompson, "A fundamental derivative in gasdynamics," Phys. Fluids **14**, 1843 (1971).
[20] A. Kluwick, "Interacting laminar boundary layers of dense gases," in *Fluid- and Gasdynamics*, edited by G. H. Schnerr, R. Bohning, W. Frank, and K. Bühler (Springer, Vienna, 1994), pp. 335–349.
[21] M. S. Cramer, S. T. Whitlock, and G. M. Tarkenton, "Transonic and boundary layer similarity laws in dense gases," J. Fluids Eng. **118**, 481–485 (1996).
[22] M. Pini and C. De Servi, "Entropy generation in laminar boundary layers of non-ideal fluid flows,"in *International Seminar on Non-Ideal Compressible-Fluid Dynamics for Propulsion & Power* (Springer, 2020), pp. 104–117.
[23] L. Sciacovelli, P. Cinnella, C. Content, and F. Grasso, "Dense gas effects in inviscid homogeneous isotropic turbulence," J. Fluid Mech. **800**, 140–179 (2016).
[24] L. Sciacovelli, P. Cinnella, and F. Grasso, "Small-scale dynamics of dense gas compressible homogeneous isotropic turbulence," J. Fluid Mech. **825**, 515–549 (2017).
[25] L. Duan, Q. Zheng, Z. Jiang, and J. Wang, "Dense gas effect on small-scale structures of compressible isotropic turbulence," Phys. Fluids **33**, 115113 (2021).
[26] C. Zhang, Z. Yuan, L. Duan, Y. Wang, and J. Wang, "Dynamic iterative approximate deconvolution model for large-eddy simulation of dense gas compressible turbulence," Phys. Fluids **34**, 125103 (2022).
[27] A. Vadrot, A. Giauque, and C. Corre, "Analysis of turbulence characteristics in a temporal dense gas compressible mixing layer using direct numerical simulation," J. Fluid Mech. **893**, A10 (2020).
[28] A. Vadrot, A. Giauque, and C. Corre, "Direct numerical simulations of temporal compressible mixing layers in a Bethe–Zel'dovich–Thompson dense gas: Influence of the convective Mach number," J. Fluid Mech. **922**, A5 (2021).
[29] L. Sciacovelli, P. Cinnella, and X. Gloerfelt, "Direct numerical simulations of supersonic turbulent channel flows of dense gases," J. Fluid Mech. **821**, 153–199 (2017).
[30] L. Sciacovelli, X. Gloerfelt, D. Passiatore, P. Cinnella, and F. Grasso, "Numerical investigation of high-speed turbulent boundary layers of dense gases," Flow, Turbul. Combust. **105**, 555–579 (2020).
[31] X. Gloerfelt, A. Bienner, and P. Cinnella, "High-subsonic boundary-layer flows of an organic vapour," J. Fluid Mech. **971**, A8 (2023).
[32] P. Cinnella and X. Gloerfelt, "Insights into the turbulent flow of dense gases through high-fidelity simulations," Comput. Fluids **267**, 106067 (2023).
[33] M. Thol, F. Dubberke, G. Rutkai, T. Windmann, A. Köster, R. Span, and J. Vrabec, "Fundamental equation of state correlation for hexamethyldisiloxane based on experimental and molecular simulation data," Fluid Phase Equilib. **418**, 133–151 (2016).

[34]E. W. Lemmon, I. H. Bell, M. L. Huber, and M. O. McLinden, "NIST standard reference database 23: Reference fluid thermodynamic and transport properties-REFPROP, version 10.0" (National Institute of Standards and Technology, 2018); available at https://www.nist.gov/srd/refprop
[35]W. F. Hughues and J. A. Brighton, *Fluid Dynamics (Schaum's Outline Series)*, 2nd ed. (McGraw-Hill, 1983).
[36]A. P. S. Wheeler, R. D. Sandberg, N. D. Sandham, R. Pichler, V. Michelassi, and G. Laskowski, "Direct numerical simulations of a high-pressure turbine vane," J. Turbomach. **138**, 071003 (2016).
[37]T. Cebeci, *Convective Heat Transfer*, Convective Heat Transfer (Horizons Publications, 2002).
[38]T. Cebeci and A. M. O. Smith, *Analysis of Turbulent Boundary Layers*, Applied Mathematics and Mechanics No. 15 (Academic Press, New York, 1974).
[39]R. Span and W. Wagner, "A new equation of state for carbon dioxide covering the fluid region from the triple-point temperature to 1100 K at pressures up to 800 MPa," J. Phys. Chem. Ref. Data **25**, 1509–1596 (1996).
[40]C. K. W. Tam and J. C. Webb, "Dispersion-relation-preserving finite difference schemes for computational acoustics," J. Comput. Phys. **107**, 262–281 (1993).
[41]T. J. Poinsot and S. K. Lele, "Boundary conditions for direct simulations of compressible viscous flows," J. Comput. Phys. **101**, 104–129 (1992).
[42]A. P. S. Wheeler and R. D. Sandberg, "Numerical investigation of the flow over a model transonic turbine blade tip," J. Fluid Mech. **803**, 119–143 (2016).
[43]P. J. Przytarski and A. P. S. Wheeler, "Accurate prediction of loss using high fidelity methods," J. Turbomach. **143**, 031008 (2021).
[44]A. P. S. Wheeler, "High fidelity simulation of dense vapour flows," in Proceedings of the 33rd International Conference on Parallel Computational Fluid Dynamics, Alba, Italy, 2022.
[45]J. Poggie, N. J. Bisek, and R. Gosse, "Resolution effects in compressible, turbulent boundary layer simulations," Comput. Fluids **120**, 57–69 (2015).
[46]F. H. Clauser, *The Turbulent Boundary Layer* (Elsevier, 1956), pp. 1–51.
[47]P. R. Spalart and J. H. Watmuff, "Experimental and numerical study of a turbulent boundary layer with pressure gradients," J. Fluid Mech. **249**, 337–371 (1993).
[48]SURF, "Dutch National Supercomputer Snellius" (2023), available at https://www.surf.nl/en/services/snellius-the-national-supercomputer.
[49]L. J. Jardine and R. J. Miller, "The effect of heat transfer on turbine performance," in ASME Turbo Expo: Turbomachinery Technical Conference and Exposition, 2019.
[50]T. Chen, B. Yang, M. C. Robertson, and R. F. Martinez-Botas, "Direct numerical simulation of real-gas effects within turbulent boundary layers for fully-developed channel flows," J. Global Power Propul. Soc. **5**, 216–232 (2021).